

A ONE-DIMENSIONAL SHOCK-CAPTURING MODEL FOR LONG WAVE RUN-UP ON VEGETATED AND NON-VEGETATED BEACHES

Soumendra Nath Kuiry¹, Weiming Wu², Yan Ding³

Abstract

This paper presents a one-dimensional, finite volume model to investigate long wave run-up under non-breaking and breaking conditions and attenuation due to vegetation. A conservative form of the non-linear shallow water equations is solved using a high-resolution Godunov-type scheme coupled with HLL Riemann solver. The effects of vegetation are modeled in the form of drag and inertia forces as the source terms in the momentum equation. The surface gradient method leads to a well-balanced formulation between the flux and the source terms. The explicit time discretization is first-order accurate but a piecewise linear reconstruction of numerical data at cell interfaces helps achieve second-order accuracy in space. The model accurately describes propagation of non-breaking and breaking waves on a sloping beach. The computed surface elevation, flow velocity, run-up and attenuated wave height show very good agreement with available analytical solutions and experimental observations.

Key words: Shallow water, Shock-capturing, Solitary waves, Breaking waves, Wave run-up, Vegetation, Wave attenuation

¹ Ph. D., Research Scientist, National Center for Computational Hydroscience and Engineering, The University of Mississippi, University, MS 38677, Email: *snkuiry@ncche.olemiss.edu*

² Ph. D., Research Associate Professor, National Center for Computational Hydroscience and Engineering, The University of Mississippi, University, MS 38677, Email: *wuwm@ncche.olemiss.edu*

³ Ph. D., A. M. ASCE, Research Assistant Professor, National Center for Computational Hydroscience and Engineering, The University of Mississippi, University, MS 38677, Email: *ding@ncche.olemiss.edu*

1 Introduction

Shallow water long waves, such as tides, storm surges and tsunamis may develop large amplitudes in coastal water and inundate low-lying areas causing casualties and damage to properties. The recent trends on protecting shoreline from such long waves are primarily focusing more on non-intrusive measures such as vegetation. Vegetation protects the shoreline through the root systems and enhances the storage of sand in dunes [1]. Nevertheless, vegetation offers resistance to the incident waves causing wave attenuation by dissipating energy and sediment deposition in the vegetated regions. Thus, vegetation plays a significant role on wave run-up and attenuation and shoreline stability. Therefore, wave run-up and interaction between water wave and vegetation needs to be quantified.

A considerable research effort has been devoted over the years to the development of analytical and numerical models to predict wave run-up and attenuation due to vegetation. Generally, effects of vegetation are included in a wave run-up model as a resistance force. In this study our concern is to develop a one-dimensional model which can simulate run-up for breaking and non-breaking waves and is able to simulate wave attenuation due to vegetation. A brief literature review on wave run-up models and the models that consider vegetation effects are discussed separately in the following two paragraphs.

The important aspects of wave run-up can be simulated through the solitary wave representation. Notable analytical results include the one-dimensional solution of **Carrier and Greenspan [2]**. **Synolakis [3]** conducted a series of experiments to understand the physical processes and proposed analytical solutions to compute run-up on a sloping beach. However, the existing analytical run-up models based on the non-linear shallow water equations (NSWEs) are restricted to the propagation of non-breaking waves on simple beach geometries [2-4]. As a long wave approaches shallow water, its wavelength and energy are compressed and its amplitude increases. In this region non-linearities lead to steepening waves, propagating bores or even breaking waves. Only the integral form of the NSWEs is valid near discontinuities and modeling this regime accurately requires numerical scheme that can handle steep gradients and discontinuities. When dealing with discontinuities, volume conservation becomes an important factor for models based on non-conservative, differential form of the NSWEs. The finite volume

method has the advantage of solving integral form of the equations as a fully conservative scheme. The Godunov-type formulation with Riemann solver can handle steep gradients through shock-capturing ability. These models can simulate wave run-up for both breaking and non-breaking waves. **Dodd [5]** investigated wave run-up, overtopping and regeneration problem using the approximate Riemann solver of **Roe [6]** and resolved the moving boundary value problem by imposing a minimum water depth criteria in the dry area. **Hu et al. [7]** presented a similar model based on the Harten, Lax and van Leer (HLL) approximate Riemann solver **[8]**. **Brocchini et al. [9]** applied finite volume method to two-dimensions using weighted average flux method with an exact Riemann solver and the moving shoreline was treated as a cavitation problem. **Wei et al. [10]** presented a run-up model in two-dimensions using an exact Riemann solver. **Delis et al. [11]** developed one- and two-dimensional run-up models based on Roe's Riemann solver and improved wet/dry algorithm. **Mahdavi and Talebbeydokhti [12]** proposed a one-dimensional wave run-up model for breaking and non-breaking waves using a first-order centered scheme (FORCE).

In general, wave attenuation is caused by energy loss through the work performed on the plants **[13]**. **Price et al. [14]** developed a hydrodynamic model that simulates the effects of seaweed as a high viscous layer. **Mork [13]** extended the idea of high viscous layer and developed a theory to take into account the form drag for the canopy layer and the lower vegetative area. **Camfield [15]** considered vegetation as a high friction area and studied wind-wave growth over shallow flooded regions. Numerous models predict wave attenuation using time-averaged conservation equation of wave energy and account for vegetation effects in an energy dissipation term **[16, 17]** while others use the conservation of momentum approach **[18, 19]**. **Mendez et al. [20]** modified the wave damping theories proposed in **[18]** and **[21]** to include random waves.

The primary goal of the present study is to develop a one-dimensional hydrodynamic model for simulating breaking and non-breaking wave run-up over vegetated and non-vegetated beaches and investigating the effect of vegetation on wave attenuation. The study makes use of a Godunov-type scheme with the HLL Riemann solver to track the moving waterline and to capture flow discontinuities associated with bores or breaking waves, which are essential for run-up calculations. The effects of vegetation are included in the form of drag and inertia forces in the momentum equations **[22]**. Previous analytical, numerical and experimental results provide

case studies for model verification and validation. Surface elevation, flow velocity, run-up, and attenuated wave height comparisons indicate the excellent performance of the present model.

2 Governing equations

As a solitary wave approaches toward the nearshore, the wave length becomes shorter and the amplitude becomes larger. Therefore, the effects of wave non-linearity become increasingly dominant. The NSWs in one-dimension may sufficiently be used for the behaviours of long waves, provided that the effects of frequency dispersion remain negligible in the nearshore zone. When the resistance offered by vegetation is also considered, the shallow water equations take the following conservative form:

$$\frac{\partial \mathbf{U}}{\partial t} + \frac{\partial \mathbf{F}}{\partial x} = \mathbf{S} \quad (1)$$

where \mathbf{U} = vector of conserved variables, \mathbf{F} = convective flux vector and \mathbf{S} = source term vector, defined as

$$\mathbf{U} = \begin{bmatrix} H \\ q \end{bmatrix}, \quad \mathbf{F} = \begin{bmatrix} q \\ \frac{q^2}{h} + \frac{1}{2}gh^2 \end{bmatrix}, \quad \mathbf{S} = \begin{bmatrix} 0 \\ gh(S_0 - S_f) - F_D - F_I \end{bmatrix} \quad (2)$$

In the above equation, H = water surface level from a datum, h = depth of water (Fig. 1), q = discharge per unit width, g = gravitational acceleration, S_0 = bed slope, S_f = friction slope, F_D = drag and F_I = inertia force components per unit area induced by vegetation. Here, water level (H) is considered as one of the unknown variables instead of water depth (h) due to the fact that reconstruction of h for higher-order spatial accuracy directly from the cell-averaged values will not guarantee a continuous reconstruction at the cell interfaces if the bed slope varies from cell to cell [23, 24]. The bed slope S_0 is given by

$$S_0 = -\frac{\partial z}{\partial x} \quad (3)$$

where z = bed elevation (Fig. 1). The friction slope is approximated using Manning's resistance law

$$S_f = \frac{n^2 u |u|}{h^{4/3}} \quad (4)$$

in which n and u denote the Manning's friction coefficient and velocity, respectively.

The resistance force induced by vegetation may be assumed similar to the force due to multiple piles for wave-current force as suggested in [25]. The total resistance force due to vegetation under wave action can be splitted into two terms [22]: (a) drag force and (b) inertia force. The drag force is due to viscous effect and the wake formation downstream of the stem. The inertia force is due to the buoyancy force on the stem as well as the fluid acceleration around the stem arising from the local pressure gradient. In absence of wave, the inertia force in Eq. (2) is negligible. The following expressions define these forces per unit area:

$$F_D = \frac{1}{2} C_D N_v A_v u |u| \quad (5)$$

$$F_I = C_I N_v A_v \min(h_v, h) \frac{\partial u}{\partial t} \quad (6)$$

where C_D = drag coefficient, C_I = inertia coefficient, N_v = number of stems per unit area, and A_v = projected area of a stem:

$$A_v = D \min(h_v, h) \quad (7)$$

in which D and h_v represent the diameter and length of the stem, respectively.

3 Numerical Solution

A cell-centered upwind finite volume method based on the Godunov-type scheme is used here to solve the NSWs. The computational domain is discretized into N control volumes termed as cells and with $N+1$ cell interfaces through which numerical fluxes are computed. The conserved

variables H and q are stored at the cell center when first-order accuracy is maintained. The integral form of Eq. (1) over a cell length, Δx , is written as

$$\int_{\Delta x} \frac{\partial \mathbf{U}}{\partial t} dx + \int_{\Delta x} \frac{\partial \mathbf{F}}{\partial x} dx = \int_{\Delta x} \mathbf{S} dx \quad (8)$$

After applying Green's theorem to Eq. (8), the update equation for a cell i appears as follows

$$\mathbf{U}_i^{n+1} = \mathbf{U}_i^n - \frac{\Delta t}{\Delta x} (\mathbf{F}_{i+1/2}^{*n} - \mathbf{F}_{i-1/2}^{*n}) + \Delta t \mathbf{S}_i^n \quad (9)$$

where $\mathbf{F}_{i+1/2}^{*n}$ = flux at cell interface $i+1/2$, Δt = time step, and n = time step index. The flux may be computed by a commonly used Riemann solver such as Roe [6] and HLL [8]. In this study, the HLL Riemann solver is chosen to compute the flux. It is preferred to Roe's Riemann solver because it better describes the flux for dry bed situation and does not require any entropy fix [26, 27].

The HLL scheme assumes one constant state between left and right waves and defines the flux at an interface as

$$\mathbf{F}_{\text{HLL}} = \begin{cases} \mathbf{F}_L & \text{if } S_L \geq 0 \\ \mathbf{F}^* & \text{if } S_L < 0 < S_R \\ \mathbf{F}_R & \text{if } S_R \geq 0 \end{cases} \quad (10)$$

in which $\mathbf{F}_L = \mathbf{F}(\mathbf{U}_L)$ and \mathbf{U}_L are the flux and conservative variable vectors evaluated at the left-hand side of each cell interface while $\mathbf{F}_R = \mathbf{F}(\mathbf{U}_R)$ and \mathbf{U}_R are the same quantities evaluated at the right-hand side. \mathbf{F}^* denotes the flux at the intermediate state, given by

$$\mathbf{F}^* = \frac{S_R \mathbf{F}_L - S_L \mathbf{F}_R + S_L S_R (\mathbf{U}_R - \mathbf{U}_L)}{S_R - S_L} \quad (11)$$

The symbols S_L and S_R represent the celerities of the waves, separating constant states of the local Riemann problem solution at cell interfaces. They can be estimated through the ‘‘two expansion’’ approach [28] as follows:

$$S_L = \min\left(u_L - \sqrt{gh_L}, u^* - \sqrt{gh^*}\right) \quad (12)$$

$$S_R = \max\left(u_R + \sqrt{gh_R}, u^* + \sqrt{gh^*}\right) \quad (13)$$

$$u^* = \frac{1}{2}(u_L + u_R) + \sqrt{gh_L} - \sqrt{gh_R} \quad (14)$$

$$\sqrt{gh^*} = \frac{1}{2}(\sqrt{gh_L} + \sqrt{gh_R}) + \frac{1}{4}(u_L - u_R) \quad (15)$$

Note that for a dry bed problem the wave speeds S_L and S_R are estimated according to the following expressions:

$$S_L = u_L - \sqrt{gh_L} \quad S_R = u_L + 2\sqrt{gh_L} \quad \text{for right dry bed} \quad (16)$$

$$S_L = u_R - 2\sqrt{gh_R} \quad S_R = u_R + \sqrt{gh_R} \quad \text{for left dry bed} \quad (17)$$

A detailed description of the scheme can be found in **Toro [27]** including a complete discussion regarding the Riemann problem in the presence of a vacuum and the reasons for a special treatment of the cells located on the wave front or shore line (wet/dry boundary).

If the intermediate states \mathbf{U}_L and \mathbf{U}_R are defined as the cell-centered values, a first-order accurate scheme is obtained, which suffers from excess numerical dissipation, and accuracy is undermined. A more accurate method can be obtained by reconstructing the variables for the left and right states, as described in the following subsection.

4 MUSCL reconstruction

The use of constant initial data in each cell for \mathbf{U}_L and \mathbf{U}_R leads to a first-order spatial accuracy. Second-order spatial accuracy is obtained by employing a Monotonic Upstream Scheme for Conservation Laws (MUSCL) reconstruction technique **[29]**. The basic idea of variable reconstruction is to replace the piecewise constant approximation of Godunov scheme by reconstructed states, derived from cell-averaged states. For each cell, the limited gradient and reconstructed left and right states are obtained and used to calculate the fluxes at the cell

interfaces. These fluxes in turn are used as input to the Riemann solver. Usually, a piecewise linear reconstruction is used:

$$\mathbf{U}_{i+1/2}^L = \mathbf{U}_i + \frac{\Delta x_i}{2} \left(\frac{\partial \mathbf{U}}{\partial x} \right)_i \quad (18)$$

$$\mathbf{U}_{i+1/2}^R = \mathbf{U}_{i+1} - \frac{\Delta x_{i+1}}{2} \left(\frac{\partial \mathbf{U}}{\partial x} \right)_{i+1} \quad (19)$$

The gradient across cell i is determined using the values in the neighbouring cells $i \pm 1$. Such gradient calculation often results in under/overshoots which will cause spurious oscillations in the solution. The *minmod* slope limiter is used here to eliminate under/overshoots and the limited gradients are calculated as follows:

$$\left(\frac{\partial \mathbf{U}}{\partial x} \right)_i = \text{minmod} \left(\frac{\mathbf{U}_i - \mathbf{U}_{i-1}}{x_i - x_{i-1}}, \frac{\mathbf{U}_{i+1} - \mathbf{U}_i}{x_{i+1} - x_i} \right) \quad (20)$$

The minmod function is defined as the argument with smaller value if all arguments have the same sign and otherwise it is zero. Once the variables on left and right sides of cell interfaces are evaluated, the fluxes are calculated using Eq. (10) with these modified variable values.

The reconstruction of variable, h , needs special attention otherwise water will accelerate under still water condition. In order to satisfy still water condition, instead of reconstructing water depth (h), the water surface level (H) measured from a datum is reconstructed following the Surface Gradient Method (SGM) as proposed by [Zhou et al. \[24\]](#). The water depth at the interface is then calculated simply by subtracting bed elevation at the interface from the reconstructed water level. Thus, this method includes the influence of bed topography while reconstructing the water depth.

5 Source terms

Bed friction, bed slope, drag and inertia forces are added as source terms in the momentum equation to consider the effect of bed resistance, topography and vegetation. It is convenient to

discretize the bed friction, drag and inertia terms semi-implicitly in order to make the diagonal dominant and subsequently to increase model stability. The semi-implicit treatment of these three terms is expressed as

$$\int_{\Delta x} S_f dx = S_f \Delta x = \left(\frac{n^2 |u^n|}{(h^{4/3})^n} \Delta x \right) u^{n+1}$$

$$\int_{\Delta x} F_D dx = F_D \Delta x = \left(\frac{1}{2} C_D N_V A_V^n |u^n| \Delta x \right) u^{n+1}$$

$$\int_{\Delta x} F_I dx = F_I \Delta x = \left(C_I N_V A_V^n \min(h_V^n, h^n) \Delta x \right) \frac{u^{n+1} - u^n}{\Delta t}$$

The bed slope treatment needs special attention as improper discretization leads to imbalance with hydrostatic flux under still water condition. The present study discretizes the bed slope term in a simple way with a well balanced scheme [23, 24, 30, 31]. Also, the authors have found that higher-order reconstruction of water depth is required to calculate hydrostatic flux accurately, as discussed below.

The bed slope term takes the following form after integration over the length of a cell

$$S_b = g \int h S_0 dx = -g \int h \frac{\partial z}{\partial x} dx \quad (21)$$

The treatment of the term in Eq. (21) has to be done in such a way that it does not artificially accelerate the flow in the limit of still water condition, that is, $q = 0$ as $\partial H / \partial x = 0$. In the absence of flows through the boundaries, the momentum equation reduces to

$$\oint \left(\frac{1}{2} g h^2 \right) dx = -g \int_{\Delta x} h \frac{\partial z}{\partial x} dx \quad (22)$$

This indicates that the sum of the hydrostatic pressure forces at the interfaces of a cell in the longitudinal direction is numerically equal to the weight component of the water contained within the cell in the same direction. The following paragraphs describe evaluation of the two

terms, the weight of water and the hydrostatic pressure force, for a cell that satisfies Eq. (22) exactly under still water condition.

The net hydrostatic pressure force (P_i) acting at the two interfaces of cell i shown in Fig. 2 is given by

$$P_i = P_2 - P_1 = \frac{1}{2} \rho g h_{i+1/2}^2 - \frac{1}{2} \rho g h_{i-1/2}^2 = \frac{1}{2} \rho g (h_{i+1/2}^2 - h_{i-1/2}^2) \quad (23)$$

In the HLL solver, interface fluxes are calculated based on one of three possible formulae in Eq. (10), depending on the local wave speed at the cell interface. However, because $\partial H / \partial x = 0$ and thus $H = \text{constant}$ for a wet bed application, it is trivial to prove that the interface fluxes are nothing but the hydrostatic pressure forces at the interfaces no matter which calculation formula is used. Therefore, Eq. (23), when divided by ρ , represents the discretized form of the left hand side of Eq. (22).

Consider a cell with inclined water surface on a sloped bed as shown in Fig. 2. The longitudinal component of weight of water in the cell can be written as

$$W_i = w_i \sin \alpha \approx w_i \tan \alpha = (\rho g h_i \Delta x) \left(-\frac{z_{i+1/2} - z_{i-1/2}}{\Delta x} \right) = -\rho g h_i (z_{i+1/2} - z_{i-1/2}) \quad (24)$$

where w_i = weight of water in the cell i , h_i = depth at the centroid of cell i and α = angle made by the bed with the horizontal. Eq. (24), when divided by ρ , represents the discretized form of the right-hand side of Eq. (22). The SGM proposed by **Zhou et al. [24]** assumes that the water depth at the centroid of a cell may be approximated as the arithmetic average of the water depths at the two interfaces, i.e., $h_i = (h_{i+1/2} + h_{i-1/2}) / 2$. Now, Eq. (24) may be written as

$$W_i = -\rho g h_i (z_{i+1/2} - z_{i-1/2}) = -\rho g \frac{h_{i+1/2} + h_{i-1/2}}{2} (z_{i+1/2} - z_{i-1/2}) \quad (25)$$

The bed elevations in Eq. (25) can be replaced by the following expressions

$$z_{i+1/2} = H_{i+1/2} - h_{i+1/2} \quad \text{and} \quad z_{i-1/2} = H_{i-1/2} - h_{i-1/2} \quad (26)$$

where $H_{i\pm 1/2}$ define water levels at the interfaces $i \pm 1/2$ of the cell i . The substitution of Eq. (26) into Eq. (25) produces

$$W_i = \frac{1}{2} \rho g (h_{i+1/2}^2 - h_{i-1/2}^2) - \Delta w_i \quad (27)$$

where

$$\Delta w_i = \frac{1}{2} \rho g (h_{i+1/2} + h_{i-1/2}) (H_{i+1/2} - H_{i-1/2}) = \rho g h_i (H_{i+1/2} - H_{i-1/2}) \quad (28)$$

When the velocity is zero and the water surface is horizontal ($H_{i+1/2} = H_{i-1/2} = H_i$), Eq. (27) reduces exactly to that given by Eq. (23) since Δw_i given by Eq. (28) vanishes and the still water condition is guaranteed to be satisfied. Therefore, the proposed method balances the flux gradients and source terms when the pressure terms are evaluated at cell interfaces and the bed slope term is directly evaluated as suggested in Eq. (24) instead of the more complicated upwind approach (e. g. [32, 33]).

It may be observed that for flowing water with a general inclined water surface, the weight component of the water contained in a cell i , W_i [Eq. (27)], differs from the respective net hydrostatic pressure force, P_i [Eq. (23)], by an amount given by Δw_i [Eq. (28)]. A second-order approximation of the water surface, thus, captures this net difference of forces within a cell. However, a first-order approximation neglects this difference, as it considers a horizontal water surface within a cell to evaluate the pressure force terms though this difference may not always be negligible. Therefore, the authors would like to point out that the first-order accurate schemes fail to compute pressure force accurately and the hydrostatic pressure forces should be calculated based on the water depths at cell interfaces.

6 Boundary conditions

The proposed model is designed to work for subcritical and supercritical flow boundary conditions. When wave is imposed as a time series of water level and wave reflection takes place, a non-reflecting wave inlet boundary condition is implemented. The moving shoreline is defined as wetting/drying of boundary cells. Various types of boundary conditions used in the present model are discussed briefly in the following subsections.

6.1 Subcritical and supercritical flow boundary conditions

For a well-defined solution of Eq. (1), two external boundary conditions are needed. They are implemented according to the flow regime at the boundaries. For subcritical flows, one boundary condition must be specified at each of the inflow and outflow boundaries. For supercritical flows, two boundary conditions are required at inflow side, and none at the downstream side. If one of the flow variables (H or q) is prescribed at one of the boundaries, then a solution for the other dependent variable is found using the method of characteristics (MOC) [34, 35]. Assuming that we can neglect the source terms and that the flux has the frontal behavior, the Riemann invariants for one-dimensional shallow water equations can be written as

$$\begin{aligned} \frac{d}{dt} R^+ = \frac{d}{dt}(u + 2c) = 0 \quad \text{on} \quad \frac{dx}{dt} = u + c \\ \frac{d}{dt} R^- = \frac{d}{dt}(u - 2c) = 0 \quad \text{on} \quad \frac{dx}{dt} = u - c \end{aligned} \tag{29}$$

Such that $u \pm 2c$ is constant along $u \pm c$, respectively. Here, c is the local wave speed given by $c = \sqrt{gh}$. The forward characteristic (R^+) is used at the end of the reach and the backward characteristic (R^-) is used at the inlet to find out the unknown variables at the boundaries.

6.2 Transmissive boundary condition

A transmissive boundary, also known as transparent boundary, allows a wave to pass through the boundary completely without any reflection. This boundary condition is efficiently implemented by adding ghost cells and assigning the conserved variables on the ghost cells the same values as those on the neighbouring cells inside the domain [7].

6.3 Non-reflecting wave inlet boundary condition

In the wave run-up and run-down processes on a beach, time series of wave heights or wave height as a function of time are often prescribed at the ocean boundary. There is a possibility that reflective waves may be generated and pass through the inlet boundary, interfering with the

incident waves. In this case, a non-reflecting wave condition at the inlet boundary is required so that the reflected waves can pass through without carrying any disturbance back to the computational domain. The second-order characteristic approach proposed by **Hu et al. [7]** is implemented in this study. The method is based on the long wave assumption and the inlet boundary has to be located beyond the break point so that the flow at the boundary is subcritical.

6.4 Moving boundary on the shoreline

The wave run-up and run-down processes on a beach can be categorized as moving boundary problem that can be viewed as wetting and drying of boundary cells. The HLL solver is preferred in this study because of the better description of numerical flux through the wet/dry interface. In the drying/wetting procedure a local minimum water depth, h_{tol} is specified. At each time step the cells are checked for dry and wet definition. The cells having water depths less than h_{tol} and without any wet neighbouring cell are defined as dry. These dry cells are not considered in the computation. Therefore, in each time step the moving boundary is defined as the line of separation between wet and dry cells. The flux through the wet-dry interface is calculated using the standard formulation presented in Section 3. However, special attentions are given for two possible situations when a wet cell is adjacent to a dry cell (a) where the water level in the wet cell is lower than the bed level of the dry cell, wetting is impossible and the mass flux and the dynamic component of the momentum are zero. To overcome this problem, the wet cell velocity for the evaluation of the flux component through the wet-dry interface is set to zero and the water surface level of the dry cell is temporarily set equal to the water level of the wet cell. (b) for the case where the water level in the wet cell is higher than the water level in the dry cell, the flow continues to flood the dry cell. When the bed slope is steep, there is possibility that more water than is actually contained in the wet cell could be computed as flowing into the dry cell, causing water depth in the wet cell to become negative. Such flow condition may be handled as described in **[36]**. However, this approach needs extra computations and book keeping of the variables which may not be necessary. For simplicity, if the water depth in a cell falls below the threshold water depth, then it will be reset to h_{tol} and the velocity is set to zero. Though this approach may add extra mass in the system but is found to be negligible **[7, 37]**. This is a relatively simple and effective approach to track the moving boundary.

7 Numerical tests

The proposed model is tested rigorously in different flow conditions. First, the model is tested against analytical solutions to examine the accuracy of the proposed shock-capturing model. Then the model is tested for laboratory cases such as flow over a triangular obstacle and solitary wave run-up on a non-vegetated sloping beach and flow through a vegetated laboratory flume. Finally, the effect of vegetation on wave attenuation is investigated by simulating hypothetical cases of wave run-up on vegetated and non-vegetated beaches.

7.1 Transcritical flow with shock over a bump

A series of tests were performed in the workshop on dam-break wave simulations (e. g. [38]) in order to evaluate the ability of numerical schemes to correctly represent the critical transitions and to validate the treatment of source terms as it involves spatially varying bottom topography.

The spatial domain is represented by a 25×1 m rectangular cross section channel (discretized as $\Delta x = 0.1$ m). The channel is frictionless and bottom topography is described by the following function:

$$z(x) = \begin{cases} 0 & \text{for } x \leq 8 \text{ m} \\ 0.2 - 0.05(x-10)^2, & \text{for } 8 < x < 12 \text{ m} \\ 0 & \text{for } x \geq 12 \text{ m} \end{cases}$$

According to the initial and boundary conditions, the flow may be subcritical, transcritical with or without shock, or supercritical. The time step used for all the simulations is 0.01 s. All the numerical tests performed in [38] were simulated, but results are presented only for the steady transcritical flow with a jump, which is the most challenging to a numerical model.

The upstream inflow discharge per unit width is set to a constant value of $0.18 \text{ m}^2 \text{ s}^{-1}$ and the downstream water depth is fixed at 0.33 m. Fig. 3 (a) shows the comparison of the numerical and analytical solutions of water surface elevation along the channel at steady state. The shock position is seen to be accurately captured. However, a maximum deviation of 23.6% in discharge, shown in Fig. 3 (b), between numerical and analytical values is observed at the location of shocks. Similar differences have also been obtained by other researchers reported as

10% by **Zhou et al. [24]**, 23% by **Valiani and Begnudelli [39]** and **15% by Brufau et al. [40]**. It is worth stressing that an error on the discharge does not imply errors on mass conservation and hence the behaviour of the system may be considered very good **[39]**.

7.2 Dam break on dry and wet beds

The aim of this test case is to study the ability of the model to simulate discontinuous flow and the front wave propagation over dry bed. Consider a horizontal and frictionless channel of 1200 m long and 1 m wide, a column of water is separated by a dam located at $x = 500$ m. This test case is simulated for both wet and dry bed situations. The initial upstream water depth is 10 m and the downstream water depth is 5 m for wet bed and 0 m for dry bed. The space discretization is set at $\Delta x = 1$ m and $\Delta t = 0.01$ s. The tolerance depth for dry bed is set as $h_{tol} = 0.000001$ m. At $t = 0$ the dam is removed instantaneously. The results are reported at 30 s after the removal of the dam. The computed water surface profiles, velocities and discharges are compared with the exact solutions. Figs. 4 (a-c) compare the wet bed case and Figs. 5 (a-c) compare the dry bed case. The computed water surface profiles, velocities and the discharges closely follow the exact solutions. The exact solutions can be found in the books by **Toro [41]** and **Henderson [42]**.

7.3 Flow over a triangular obstacle

This test is carried out to reproduce the laboratory dam-break flow over a triangular hump recommended by the EU CADAM project. The physical experiment included complex hydraulic properties such as shocks, transitions between wet and dry beds and flow over an obstacle. The laboratory set up is illustrated in Fig. 6. The experiment consisted of a reservoir with water up to 0.75 m contained by a dam at $x = 15.5$ m and a dry bed downstream within a rectangular channel of 22.5 m in length. A symmetric triangular obstacle (6 m long, 0.4 m high) was placed on the channel with its peak located at 14 m downstream of the dam. In order to observe depth evolutions gauge points were located at 4 m (G4), 10 m (G10), 11 m (G11), 13 m (G13) and 20 m (G20) from the dam as shown in Fig. 6. The gauge point G13 was located at the vertex of the obstacle and therefore is a critical point. The fixed boundaries were walls except the free outlet. The Manning's roughness coefficient was supplied as $0.0125 \text{ m}^{-1/3}\text{s}$ by the experimentalists **[36]**.

In the computation, $\Delta x = 0.1$ m, $\Delta t = 0.01$ s and $h_{tol} = 0.0001$ m are used and the simulation was carried out for 90 s. The water depth variations with respect to time at the five gauge points are shown in Figs. 7 (a-e). It can be seen that the predicted water depth evolutions and arrival time of the wave are quite comparable with the measured data at most of the gauge points. The transitions from wet to dry at the gauge point G13 is well predicted. Small discrepancy is observed at G20 (after the hump) between the numerical and measured values in terms of water depth, which is also predicted by other researchers using different numerical schemes (e.g. [40], [43]).

Overall, the comparison between the numerical predictions and measurements is satisfactory and the wet–dry transitions are simulated with very high accuracy by the current model. This confirms the effectiveness of the current method on flux and source term balancing and friction term discretization.

7.4 Wave run-up in non-vegetated channel

7.4.1 Sine wave run-up on a sloping beach

A benchmark test for the validation of moving boundary condition is considered here. This case also helps to examine the accuracy of the non-reflective inlet boundary condition. The numerical model is applied to simulate run-up/run-down motion of a monochromatic wave train on a sloping beach. The model parameters are identical to those used in [44-46]. This configuration has analytical solution, which was derived by **Carrier and Greenspan [2]** using the hodograph transformation to solve the NSWs. A sine wave train with an amplitude of 0.003 m and a period of 10 s propagates in a channel with initial water depth of 0.5 m and climbs up a 1:25 sloping beach. The domain is discretized using a grid size of 0.045 m, time step of 0.005 s and $h_{tol} = 0.000001$. At the inlet, non-reflecting boundary condition is imposed to reduce the wave reflectivity. Fig. 8 compares the numerical free surface against the analytical solution of **Carrier and Greenspan [2]** for the maximum and minimum run-up; the agreement is good. This test

case proves the effectiveness of the boundary conditions and invoking a minimum water depth criteria for the drying/wetting algorithm.

7.4.2 Solitary wave run-up on a sloping beach

Synolakis [3] carried out a series of experiments to investigate run-up/run-down and breaking of a solitary wave propagating on a constant depth and sloping beach. The topography consists of a plane beach with a slope $1: \cot \beta$ adjacent to a constant depth region as shown in Fig. 9. In the schematic Fig. 9, H_w = incident wave height, β = beach angle, h_0 = still water depth. The experimental results reported in [3] have been extensively used to validate run-up models [4, 11, 12, 47, 48]. The initial conditions for the computations were a solitary wave of height H_w propagating from left to right and the wave crest is located at $\xi = X_1$. The surface profile and velocities are defined by

$$\eta(\xi, 0) = H_w \operatorname{sech}^2 \left[\sqrt{\frac{3H_w}{4h_0^3}} (\xi - X_1) \right]$$

$$u(\xi, 0) = \eta(\xi, 0) \sqrt{\frac{g}{h_0}}$$

where $h_0 = 1$ m. The crest of the initial solitary wave profile is positioned at a distance L from the toe of the beach located at X_0 , where L is the half wave length of a solitary wave defined by

$$L = \sqrt{\frac{4h_0}{3H_w}} \operatorname{arcosh} \left(\sqrt{\frac{1}{0.05}} \right)$$

For convenience, most of the results are reported in non-dimensional forms and hence, the non-dimensional variables are now introduced as

$$x^* = \frac{x}{h_0}, \quad \eta^* = \frac{\eta}{h_0}, \quad t^* = t \sqrt{\frac{g}{h_0}}$$

where η = water surface deviation from the still water level (Fig. 9).

The minimum water depth for dry bed definition is considered as 0.0001 m. A Manning coefficient of $n = 0.01$ is used to define the glass surface roughness used in the experiment. The left boundary condition is transmissive and is kept sufficiently far away from the toe of the beach in order to avoid any interaction with the water waves during the run-up process. Following examples are presented to examine the accuracy of the model to predict wave run-up for breaking and non-breaking waves based on the set up explained above.

For non-breaking solitary wave run-up, we have considered two cases for $H_w/h_0 = 0.0185$ and $H_w/h_0 = 0.04$ on a beach of slope 1:19.85. According to **Synolakis [3]**, wave breaking occurs during run-down when $H_w/h_0 > 0.044$ and hence in both cases wave breaking did not occur although the second case was very close to wave breaking during run-down. Figs. 10 (a-j) show the free surface profiles when $H_w/h_0 = 0.0185$ for different non-dimensional times. At times $t^* = 25, 30, 35$ the incident wave approached the shoreline and by time $t^* = 40$ had started its run-up on the beach. The run-down took place around $t^* = 60$. It is evident from each snapshot that the computed and observed profiles are in good agreement.

The free surface profiles at different non-dimensional times for the case of $H_w/h_0 = 0.04$ are shown in Figs. 11 (a-h). At times $t^* = 20, 26, 32$ the incident wave propagated to the shoreline and at around $t^* = 38$ had started its run-up and run-down took place around $t^* = 56$. The experimental observation at $t^* = 62$ shows that the wave nearly broke down and the numerical results look similar to that of a hydraulic jump. The numerical prediction closely follows the experimental results. The run-up and run-down tongue thickness are also well predicted.

The propagation of a non-linear breaking solitary wave with normalized incident wave height $H_w/h_0 = 0.3$ on the same beach is investigated and the results are examined against the experimental data **[3]**. Figs. 12 (a-j) shows surface profiles obtained at different non-dimensional times. At $t^* = 15, 20$ the wave shoals and the front face has become steeper earlier than the experimental wave and has changed to a bore type structure. This phenomenon may be attributed

to the limitation of non-linear shallow water equations which do not include higher-order dispersive terms to account for the non-linear effects. The experimental wave broke around $t^* = 20$ and the computed wave which represents this as a bore stores water behind the vertical front spilled from the breaking wave. The computed bore is slightly ahead of the experimental wave. The vertical front also indicates a sudden change in velocity from the bore to the undisturbed water. The breaking process terminates as the bore collapses near the shoreline. Due to volume conservation, the computation fully recovers when breaking stops at $t^* = 25$ and thereafter the attenuated wave forms a tongue propagating up the sloping beach at $t^* = 30, 35, 40, 45$. After, the wave reaches the highest point around $t^* = 45$, the run-down takes place in which a thin layer of water accelerates down to the beach and discrepancies begin to show around $t^* = 50$ as the receding supercritical flow impacts the wave tail near the still water shoreline. The finite volume model approximates this flow pattern as a hydraulic jump and conserves the flow volume behind it. The qualitative agreement between experimental and numerical profiles begins to resume gradually from $t^* = 75$, demonstrating the resilience of the model. This study shows the capability of the present model to simulate breaking and non-breaking waves on a sloping beach.

7.5 Wave attenuation in vegetated channel

7.5.1 Wave attenuation due to vegetation in a laboratory flume

The wave attenuation due to vegetation can be simulated by the proposed model when drag and inertia resistance forces induced by vegetation are considered in the governing equations. Since, the present model can simulate breaking and non-breaking wave propagation it would be interesting to see whether the same model is capable of simulating wave attenuation due to vegetation. The experiments conducted by [Asano et al. \[49\]](#) are used in this study for comparison. The schematic view of the experimental set up is shown in Fig. 13. The experiments were conducted in a wave tank that was 27 m long, 0.5 m wide and 0.7 m high. The artificial vegetation was made of polypropylene strips with specific gravity 0.9, length 0.25 m, width 0.052 m and thickness 0.3 mm. The strips were bound to a wire net at the bottom of the wave

flume. The length of vegetation field was 8 m and the number density of strips placed uniformly was 1110 and 1490 m⁻². The total water depth in the tank was ranging from 0.45 m to 0.52 m and the wave height from 0.036 m to 0.1934 m. The capacitance wave gauges were used to measure the free surface oscillations at four locations. A series of 60 test runs were conducted, out of which two are chosen for accuracy test. The same two test runs were also considered by **Li and Yan [22]** and their results are also presented here for comparison.

The numerical model has been set up to replicate the experimental conditions. The computational domain is 12 m long and 1 m wide, and $\Delta x = 0.01$ m is used. The non-reflecting boundary condition is specified at the inlet and the transmissive boundary condition is imposed at the outlet. At the inlet, a sine wave train is introduced and the simulation is carried out for long time so that a developed flow situation is achieved in the flow domain. The simulations are carried out for two different conditions (a) $H_w = 0.113$ m, period, $T = 1.25$ s, $h_0 = 0.52$ m and $N_V = 1490$ m⁻²; and (b) $H_w = 0.086$ m, $T = 2$ s, $h_0 = 0.45$ m and $N_V = 1110$ m⁻². The wave height at a point is obtained by subtracting the minimum water level from the maximum water level when dynamic steady state is reached at that point. The longitudinal wave height profiles obtained from the present model, reported by **Li and Yan [22]** and from the experiments are compared in Figs. 14 (a-b). While plotting, the origin is considered to be at the seaward side of the vegetation field. It is obvious from the figures that the wave attenuation predicted by the present model is quite satisfactory. The drag and inertia coefficients used in the simulations are $C_D = 0.75$, $C_I = 2.0$ for case (a) and $C_D = 1.0$, $C_I = 2.0$ for case (b). The values of the coefficients used in the simulations are within the ranges ($C_D \sim 1$, $C_I \sim 2$) suggested by **Li and Yan [22]**.

7.5.2 Wave attenuation due to vegetation on a sloping beach

This numerical test is performed in order to test the ability of the model to predict wave attenuation qualitatively on a vegetated sloping beach. The geometry considered is the same as shown in Fig. 9. The initial and boundary conditions are also same as described for the propagation of breaking wave for $H_w/h_0 = 0.3$. Vegetation is assumed to be from 40 m to the end of the channel. The density of vegetation is $N_V = 800$ m⁻² and diameter $D = 0.02$ m. The

drag and inertia coefficients are defined as $C_D = 1.0$, $C_I = 2.0$. The space discretization is such that each cell contains at least one stem in the longitudinal direction. In order to compare wave attenuation due to vegetation, the same set up is run for without vegetation. The Figs. 15 (a-j) compares the water surface profiles at different non-dimensional times. From the figures, it is evident that the wave is significantly attenuated due to vegetation. During $t^* = 15, 20$ wave shoals and the front face becomes steep but due to the presence of vegetation wave height is significantly reduced. The maximum wave run-up is also drastically reduced and can be seen at $t^* = 45$ when the propagating wave travels maximum distance along the beach. In absence of vegetation, at $t^* = 50$ the thin layer of run-down flow develops supercritical flow and the wave breaks in the form of hydraulic jump. But such phenomena is avoided in presence of vegetation because the propagating wave velocity is significantly retarded by vegetation. Therefore, vegetation on a sloping beach reduces the energy of the propagating wave. This reduction in energy may help to stabilize a beach by reducing soil erosion.

This hypothetical numerical test shows the ability of the model to simulate wave attenuation due to vegetation on a sloping beach. For quantitative comparison the model needs to be validated with laboratory and field data.

8 Conclusions

This paper describes the theoretical background, verification and validation of a one-dimensional shock-capturing finite volume model to predict long wave run-up and wave attenuation due to vegetation. The surface gradient method of **Zhou et al. [24]** provides a well-balanced treatment for the flux and source terms. The model uses a first-order explicit time discretization scheme and a second-order accurate space discretization through a piecewise linear reconstruction of the conserved variables. The model provides good shock-capturing property as well as accurate description of flow near the moving waterline. The effects of vegetation are included in the momentum equation as source term in the form of drag and inertia forces as suggested by **Li and Yan [22]**. The drag and inertia force expressions considers plant characteristics such as geometry, stem density, spatial coverage, buoyancy etc. to properly represent the physical processes.

The computed water depth and flow discharge are verified with analytical solutions for flow over a bump. The discrepancy in discharge at the location of shocks is common for such schemes and does not imply error in mass conservation. The model accurately predicts the water surface, velocity and discharge for an ideal dam-break on wet and dry beds. The water wave propagation due to dam-break on a dry bed with triangular obstacle is well simulated and the computed results closely follow the experimental observation. Also, the shifting of dry and wet conditions is well predicted. The hypothetical sine wave propagation on a sloping beach is simulated and the computed water surface profiles for maximum and minimum wave run-up are in good agreement with the analytical solution. Despite the limitation of depth-averaged non-linear shallow water equations, the computed free surface profiles for breaking and non-breaking wave run-up on a sloping beach are in good agreement with the experimental data of **Synolakis [3]**. The model approximates the wave breaking in the framework of bore propagation and hydraulic jump during the run-up and run-down motions, respectively. The prediction of the location of wave breaking slightly differs from the observed data and the reason may be attributed to the insufficient dispersive effects present in the governing equations. The effects of vegetation on wave attenuation are investigated by solving two test cases and comparing the results with the experimental data reported by **Asano et al. [49]**. To further test the ability of the model to simulate wave attenuation due to vegetation on a sloping beach, a hypothetical test case is introduced and the results are encouraging. The major effect of vegetation is to dissipate energy and produce attenuation of wave and the computed results show that the present model can predict wave attenuation with reasonable accuracy. The present model, therefore, despite the shallow water and wave breaking approximations, provides accurate predictions of discontinuous flows, non-breaking and breaking long wave run-up and wave attenuation due to vegetation and has potential applications in flood hazard mitigation.

Acknowledgements

This research was funded by the Department of Homeland Security-sponsored Southeast Region Research Initiative (SERRI) at the Department of Energy's Oak Ridge National Laboratory.

References:

- [1] Dean RG. Effects of vegetation on shoreline erosional processes, wetland functions and values: the state of our understanding. *Amer. Water Resour. Assoc.* 1978; 415–426.
- [2] Carrier GF, Greenspan HP. Water waves of finite amplitude on a sloping Beach. *J. Fluid Mech.* 1958; 4:97-109.
- [3] Synolakis CE. The run-up of long waves, PhD Thesis, California Institute of Technology, Pasadena, CA, 1986.
- [4] Li Y, Raichlen F. Solitary wave run-up on plane slopes. *J. Water. Port, Coast. Ocean Eng.* 2001; 127:33-44.
- [5] Dodd N. Numerical model of wave run-up, overtopping, and regeneration. *J. Water. Port, Coast. Ocean Eng.* 1998; 124:73-81.
- [6] Roe PL. Approximate Riemann solvers, parameter vectors and difference schemes. *J. Comput. Phys.* 1981; 43:357-372.
- [7] Hu K, Mingham CG, Causon DM. Numerical simulation of wave overtopping of coastal structures using the non-linear shallow water equations. *J. Coast. Eng.* 2000; 41:433–465.
- [8] Harten A, Lax PD, van Leer B. On upstream differencing and Godunov-type schemes for hyperbolic conservation laws. *SIAM Rev.* 1983; 25(1):35–61.
- [9] Brocchini M, Bernetti R, Mancinelli A, Albertini G. An efficient solver for nearshore flows based on the WAF method. *Coastal Eng.* 2001; 43(2):105-129.
- [10] Wei Y, Mao XZ, Cheung KF. Well-balanced finite-volume model for longwave run-up. *J. Water. Port, Coast. Ocean Eng.* 2006; 132:114-124.
- [11] Delis AI, Kazolea M, Kampanis NA. A robust high-resolution finite volume scheme for the simulation of long waves over complex domains. *Int. J. Numer. Fluids.* 2008; 56:419-452.
- [12] Mahdavi A, Talebbeydokhti N. Modeling of non-breaking and breaking solitary wave run-up using FORCE-MUSCL scheme. *J. Hydraul. Res.* 2009; 47(4):476-185.
- [13] Mork M. Wave attenuation due to bottom vegetation. Kluwer Academic Publishers, 1996; 371–382.
- [14] Price WA, Tomlinson KW, Hunt JN. The effect of artificial seaweed in promoting the build-up of beaches. *Proc. 11th Intern. Coast. Eng. Conf.* 1968; Vol. 1:570–578.
- [15] Camfield FE. Wind wave growth with high friction. *J. Water. Port Coast. Ocean Eng.* 1983; 109(1):115–117.
- [16] Dalrymple RA, Kirby JT, Hwang PA. Wave refraction due to areas of energy dissipation. *J. Water. Port Coast. Ocean Eng.* 1984; 110(1):67–79.
- [17] Mendez FJ, Losada IJ. An empirical model to estimate the propagation of random breaking and nonbreaking waves over vegetation fields. *Coastal Eng.* 2004; 51:103–118.
- [18] Kobayashi N, Raichlen AW, Asano T. Wave attenuation by vegetation. *J. Water. Port Coast. Ocean Eng.* 1993; 199(1):30–48.

- [19] Lima SF, Neves CF, Rosauero NML. Damping of gravity waves by fields of flexible vegetation. Proc. 30th Intern. Coast. Eng. Conf. 2006; Vol. 1:491–503.
- [20] Mendez FJ, Losada IJ, Losada MA. Hydrodynamics induced by wind waves in a vegetation field. J. Geophys. Res. 1999; 104 (C8):18383–18396
- [21] Dubi A, Torum A. Wave damping by kelp vegetation. Proc. 24th Intern. Coast. Eng. Conf. 1995; 142–156.
- [22] Li CW, Yan K. Numerical Investigation of Wave–Current–Vegetation Interaction. J. Hydraul. Eng. 2007; 133(7):794-803.
- [23] Nujic M. Efficient implementation of non-oscillatory schemes for the computation of free surface flow. J. Hydraul. Res. 1995; 33:101-111.
- [24] Zhou JG, Causon DM, Mingham CG, Ingram DM. The surface gradient method for the treatment of source terms in the shallow water equations. J. Comput. Phy. 2001; 168(1):1–25.
- [25] Morison JR, O'Brien Johnson JW, Schaaf SA. The force exerted by surface waves on piles. Petrol. Trans., AIME 1950; 189:149–157.
- [26] Fraccarollo L, Toro EF. Experimental and numerical assessment of the shallow water model for two-dimensional dam-break type problems. J. Hydraul. Res. 1995; 33(6):843–864.
- [27] Toro EF. Riemann solvers and numerical methods for fluid dynamics., 2nd Ed., Springer-Verlag, Berlin, 1999.
- [28] Toro EF. Riemann problems and the WAF method for solving the two-dimensional shallow water equations. Phil. Trans. R. Soc. Lond. 1992; A 338:43-68.
- [29] van Leer B. Towards the Ultimate Conservative Difference Scheme, V. A Second Order Sequel to Godunov's Method. J. Comput. Phys. 1979; 32:101–136
- [30] Noelle S, Xing Y, Shu, C-W. High-order well-balanced finite volume WENO schemes for shallow water equation with moving water. J. Comput. Phy. 2007; 226:29–58
- [31] Kim D-H, Cho Y-S, Kim H-J. Well-balanced scheme between flux and source terms for computation of shallow-water equations over irregular bathymetry. J. Eng. Mech. 2008; 134(4):277-290.
- [32] Bermúdez A, Vázquez ME. Upwind methods for hyperbolic conservation laws with source terms. Comput. Fluids 1994; 8:1049-71.
- [33] Vázquez-Cendón ME. Improved treatment of source terms in upwind schemes for the shallow water equations. J. Comput. Phys. 1999; 148:497-526.
- [34] García-Navarro P, Savirón J. McCormack's method for the numerical simulation of one-dimensional discontinuous unsteady open channel flow. J. hydraul. Res. 1992; 30:95-105.
- [35] Crossley AJ. Accurate and efficient numerical solutions for the Saint Venant equations of open channel flow. Ph. D. Thesis, University of Nottingham, 1999.
- [36] Brufau P, García-Navarro PA, Vázquez-Cendón ME. Zero mass error using unsteady wetting-drying conditions in shallow flows over dry irregular topography. Int. J. Numer. Methods Fluids 2004; 45:1047-82.

- [37] Que Y-T, Xu, K. The numerical study of roll-waves in inclined open channels and solitary wave runup. *Int. J. Numer. Methods Fluids* 2005; 50:1003–1027.
- [38] Goutal N, Maurel F. Technical Report HE-43/97/016/A, Electricité de France, Département Laboratoire National d'hydraulique, Groupe Hydraulique Fluviale, 1997.
- [39] Valiani A, Begnudelli L. Divergence form of bed slope source term in shallow water equations. *J. Hydraul. Eng.* 2006; 132:652-665.
- [40] Brufau P, Vázquez-Cendón ME, García-Navarro PA. (2002). Numerical model for the flooding and drying of irregular domains. *Int. J. Numer. Methods Fluids* 2002; 39:247-275.
- [41] Toro EF. *Shock-capturing methods for free-surface shallow flows*. Wiley, England, 2001.
- [42] Henderson FM. *Open channel flow*. MacMillan Company, NY, USA, 1966.
- [43] Liang Q, Marche F. Numerical resolution of well-balanced shallow water equations with complex source terms. *Adv. Water Resour.* 2009; 32:873-884
- [44] Madsen PA, Sorensen OR, Schaffer HA. Surf zone dynamics simulated by a Boussinesq-type model: Part I. Model description and cross-shore motion of regular waves. *J. Coast. Eng.* 1997; 32:255– 287.
- [45] Kennedy AB, Chen Q, Kirby JT, Dalrymple RA. Boussinesq modeling of wave transformation, breaking and runup. Part I: 1D. *J. Water., Port, Coast., Ocean Eng.* 2000; 126:39– 47.
- [46] Lynett PJ, Wu TR, Liu PL-F. Modeling wave runup with depth-integrated Equations. *J. Coast. Eng.* 2002; 46:89–107.
- [47] Zelt JA. Overland flow from solitary waves. *J. Water., Port, Coast., Ocean Eng.* 1991; 117:247-263.
- [48] Titov VV., Synolakis CE. Modeling of breaking and non-breaking long-wave evolution and run-up using VTCS-2. *J. Water., Port, Coast., Ocean Eng.* 1995; 121:308-461.
- [49] Asano T, Tsutsui S, Sakai T. Wave damping characteristics due to seaweed. *Proc., 25th Coastal Engineering Conf. in Japan* 1988; 138–142.

Notations:

The following symbols are used in this paper:

A_v	=	Projected area of a vegetation stem
C_D	=	Drag coefficient
C_I	=	Inertia coefficient
\mathbf{F}	=	Convective flux vector
F_D	=	Drag force per unit area
F_I	=	Inertia force per unit area
\mathbf{F}_{HLL}	=	HLL flux vector at an interface
\mathbf{F}_L	=	Flux vector evaluated at the left-hand side of a cell interface
\mathbf{F}_R	=	Flux vector evaluated at the right-hand side of a cell interface
g	=	Gravitational acceleration
H	=	Water surface level from a datum
H_w	=	Wave height
h	=	Depth of water
h_L, h_R	=	Water depths evaluated at the left- and right-hand sides of a cell
h_{tol}	=	Water depth tolerance to define a dry cell
h_v	=	Length of vegetation stem
h^*	=	Dimensionless water depth
h_0	=	Still water depth
i	=	Cell index
$i \pm 1/2$	=	Cell interface indices
L, R	=	Left and right sides of a cell interface
P, P_1, P_2	=	Total pressure force, pressure forces at section 1 and 2, respectively
q	=	Unit discharge
R^+, R^-	=	Forward and backward characteristics
\mathbf{S}	=	Source term vector
S_0	=	Bed slope

S_f	=	Bed friction
$S_L, S_R,$	=	Estimated wave speeds for HLL flux
$t, \Delta t, t^*$	=	Time, time step and dimensionless time
\mathbf{U}	=	Vector of conserved variables
u	=	Velocity
u^*	=	Dimensionless velocity
u_L, u_R	=	Velocities evaluated at the left- and right-hand sides of a cell interface
W	=	Weight component of water in a cell in the longitudinal direction
w	=	Weight of water in a cell
x, y	=	Cartesian coordinate
Δx	=	Cell length
x^*	=	Dimensionless length
z	=	Bed elevation from datum
α	=	Bed angle with the horizontal
β	=	Beach slope
η, η^*	=	Deviation of water surface from still water, dimensionless water surface deviation
ξ	=	Wave crest location
ρ	=	Water density

Figure Captions

Fig. 1: Schematic diagram of variables

Fig. 2: Definition sketch for force balance in a 1D control volume

Fig. 3: Transcritical flow over a bump (a): water surface; and (b): discharge

Fig. 4: Dam-break on wet bed (a): water surface; (b): velocity; and (c): discharge

Fig. 5: Dam-break on dry bed (a): water surface; (b): velocity; and (c): discharge

Fig. 6: Geometry and gauge locations in the experimental and model set up

Fig. 7: Computed and measured water depth variations at stations (a): G4; (b): G10; (c): G11; (d): G13; and (e): G20

Fig. 8: Comparison between computed free surface profiles and Carrier and Greenspan analytical solution at the maximum and minimum shoreline movements.

Fig. 9: Definition sketch for solitary wave run-up on a sloping beach

Fig. 10: Run-up of $H/h_0 = 0.0185$ non-breaking solitary wave on 1:19.85 sloping beach at different non-dimensional times t^* equal to (a): 25; (b): 30; (c): 35; (d): 40; (e): 45; (f): 50; (g): 55; (h): 60; (i): 65; and (j): 70

Fig. 11: Run-up of $H/h_0 = 0.04$ non-breaking solitary wave on 1:19.85 sloping beach at different non-dimensional times t^* equal to (a): 20; (b): 26; (c): 32; (d): 38; (e): 44; (f): 50; (g): 56; (h): 62

Fig. 12: Run-up of $H/h_0 = 0.3$ breaking solitary wave on 1:19.85 sloping beach at different non-dimensional times t^* equal to (a): 15; (b): 20; (c): 25; (d): 30; (e): 35; (f): 40; (g): 45; (h): 50; (i): 55; (j): 60; (k): 65; (l): 70; and (m): 75

Fig. 13: Schematic diagram of the laboratory experiment by Asano et al. (1988).

Fig. 14: Variation of wave height along the vegetated portion of the channel (a): case 1 [$H_w = 0.086$ m and $T = 2s$]; and (b) case 2 [$H_w = 0.113$ m and $T = 1.25s$]

Fig. 15: Wave attenuation of $H/h_0 = 0.3$ breaking solitary wave on 1:19.85 sloping beach at different non-dimensional times t^* equal to (a): 10; (b): 15; (c): 20; (d): 25; (e): 30; (f): 35; (g): 40; (h): 45; (i): 50; and (j): 55

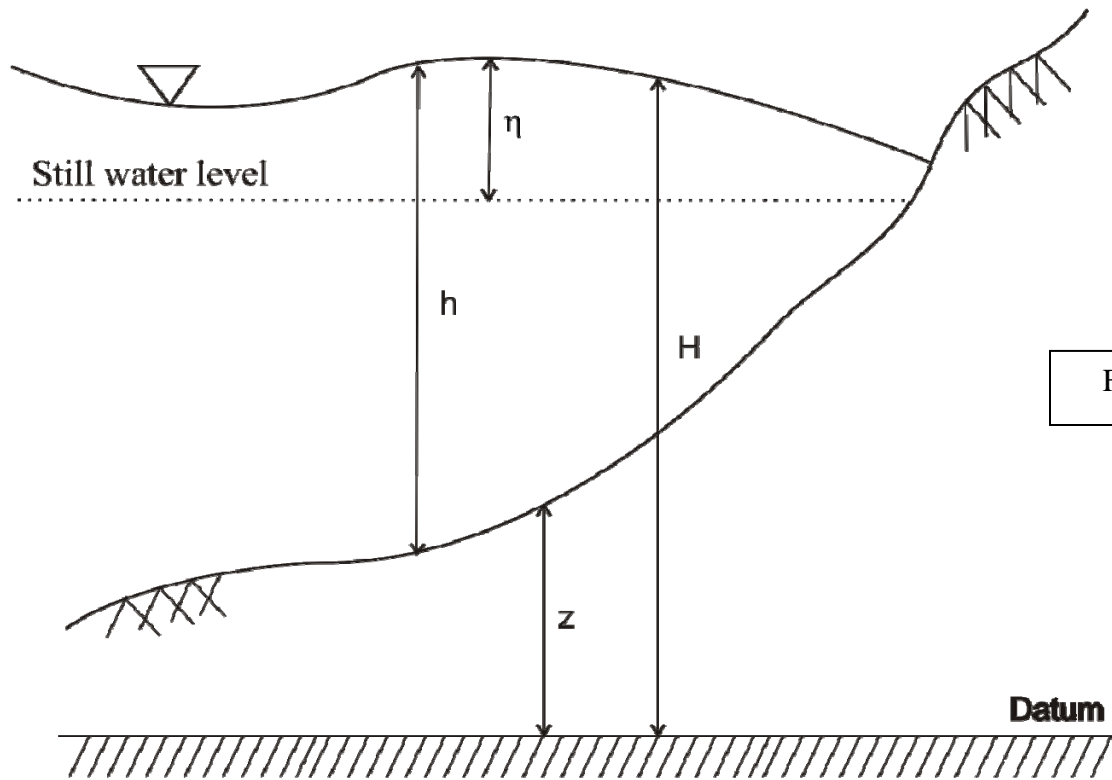


Fig. 1

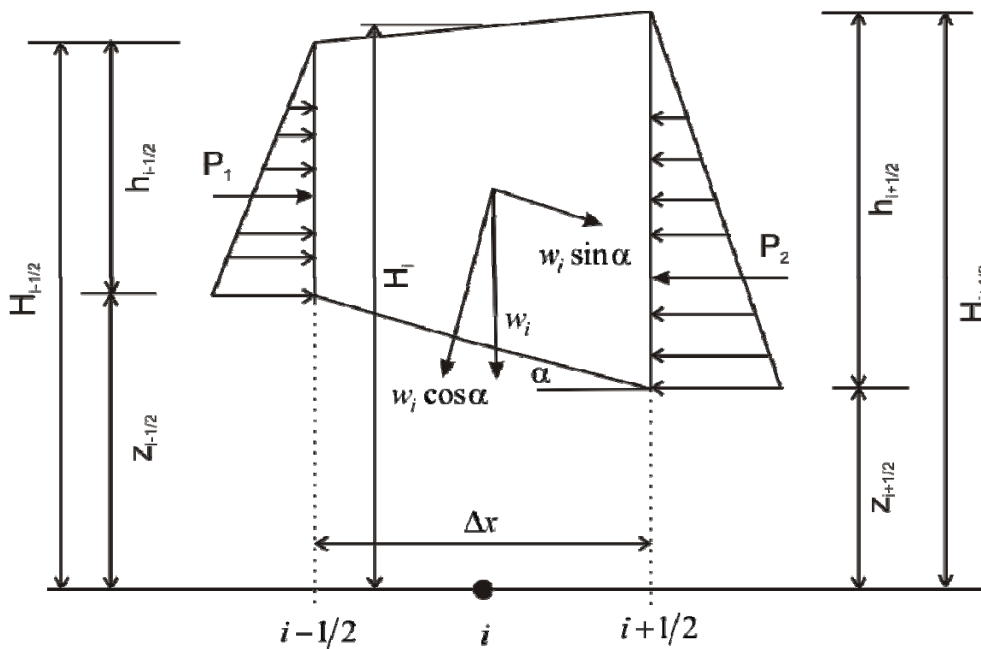


Fig. 2

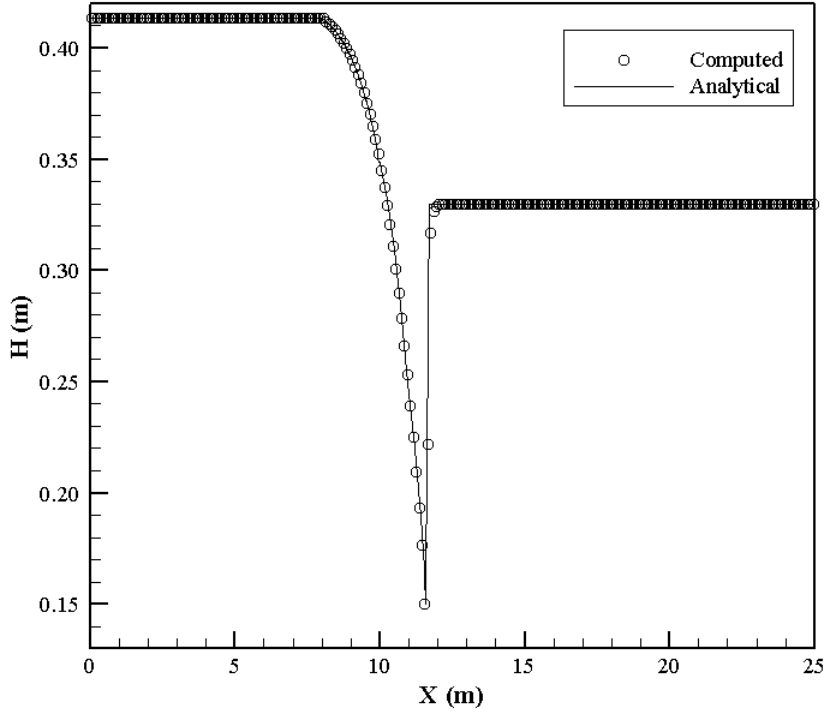


Fig. 3a

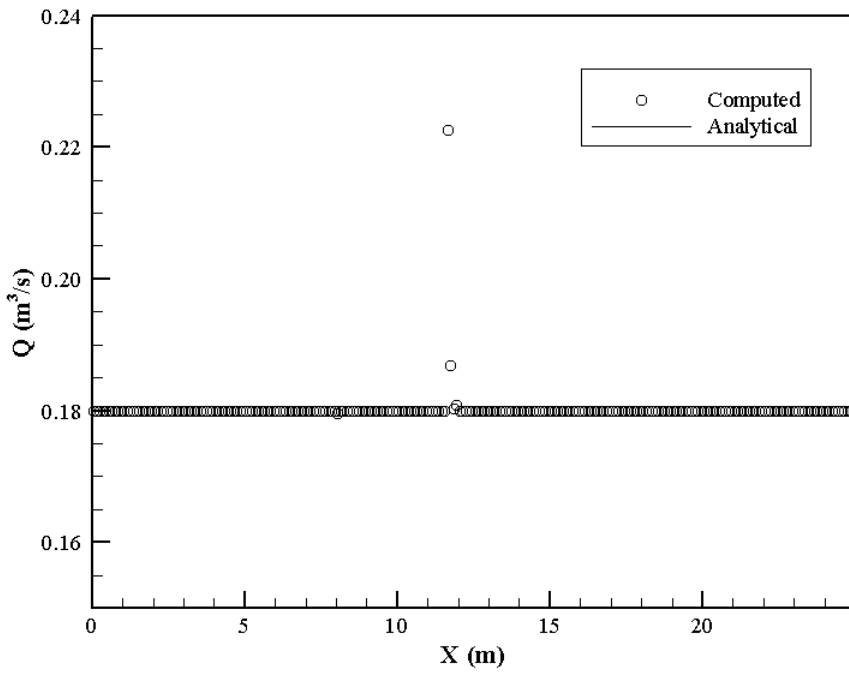


Fig. 3b

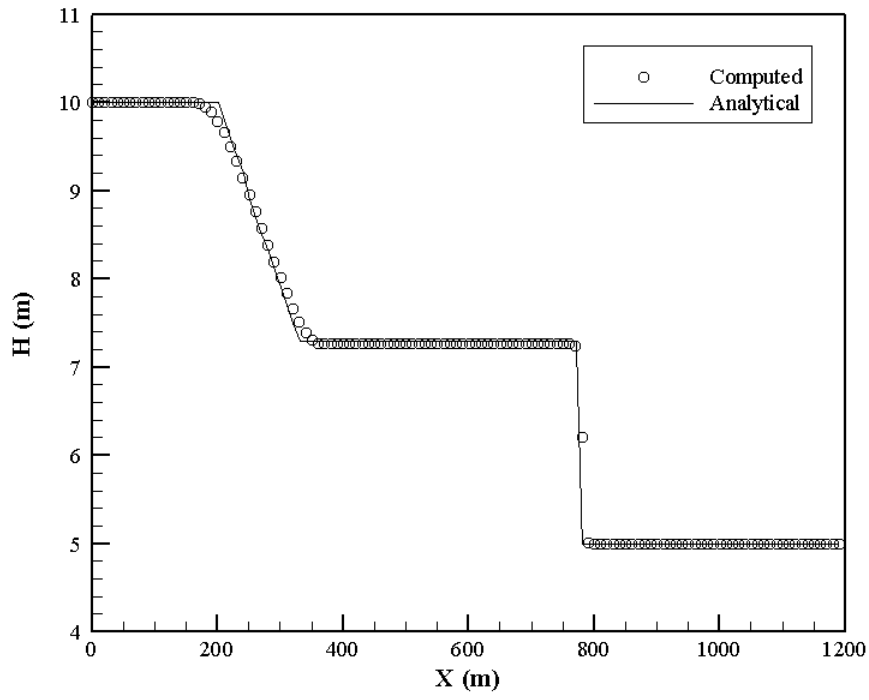


Fig. 4a

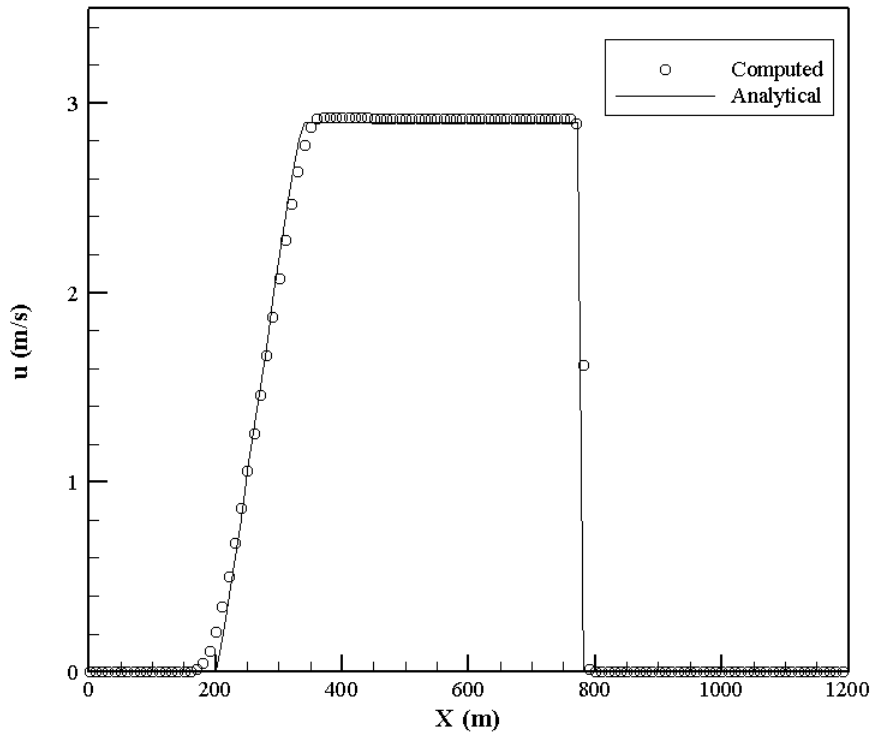


Fig. 4b

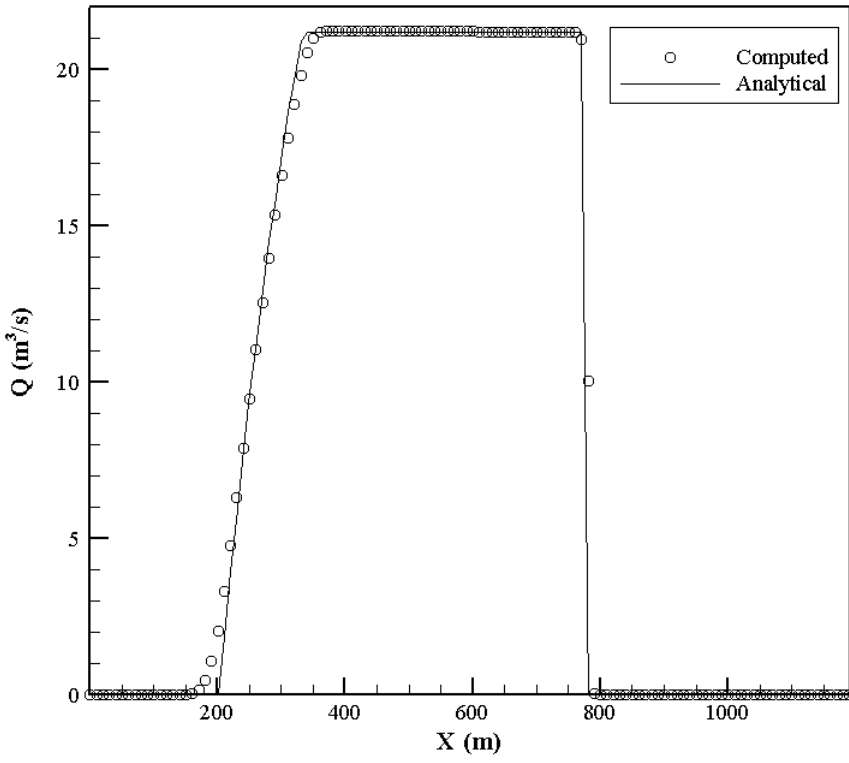


Fig. 4c

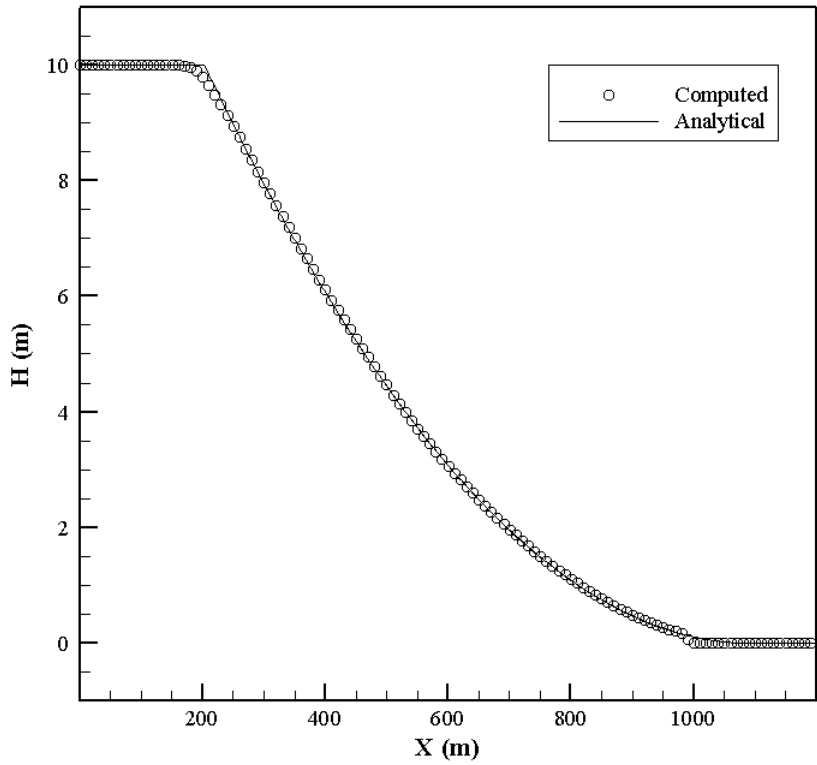


Fig. 5a

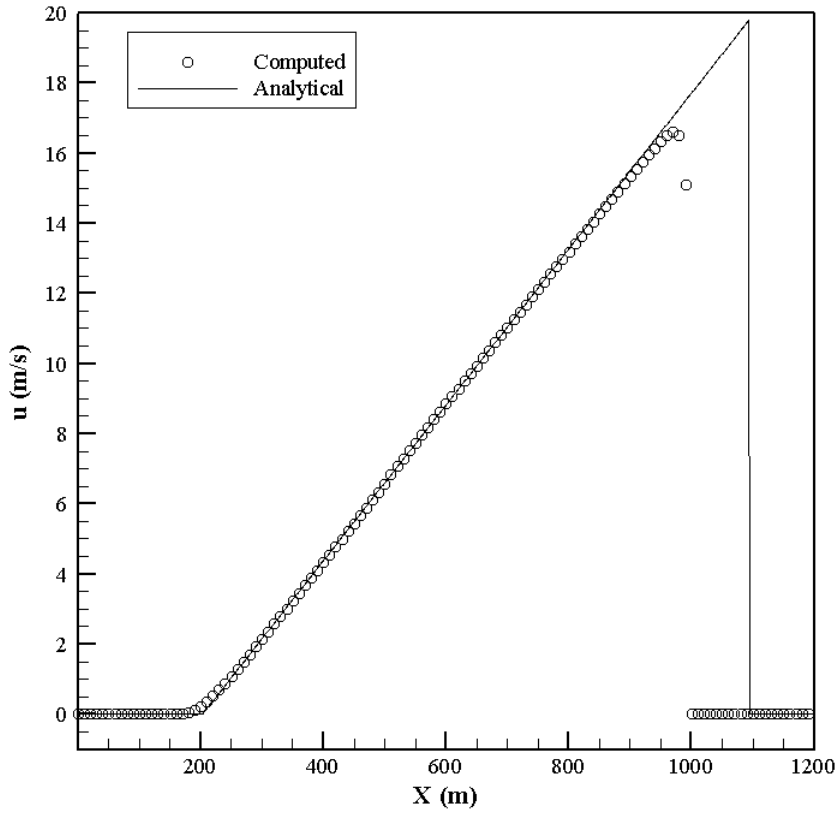


Fig. 5b

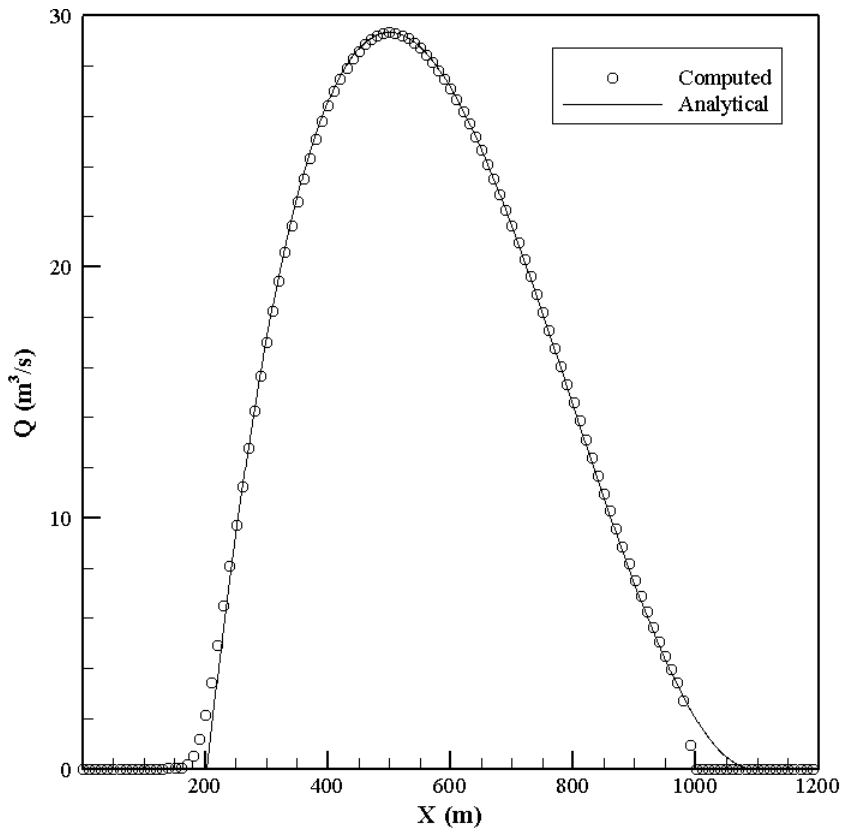


Fig. 5c

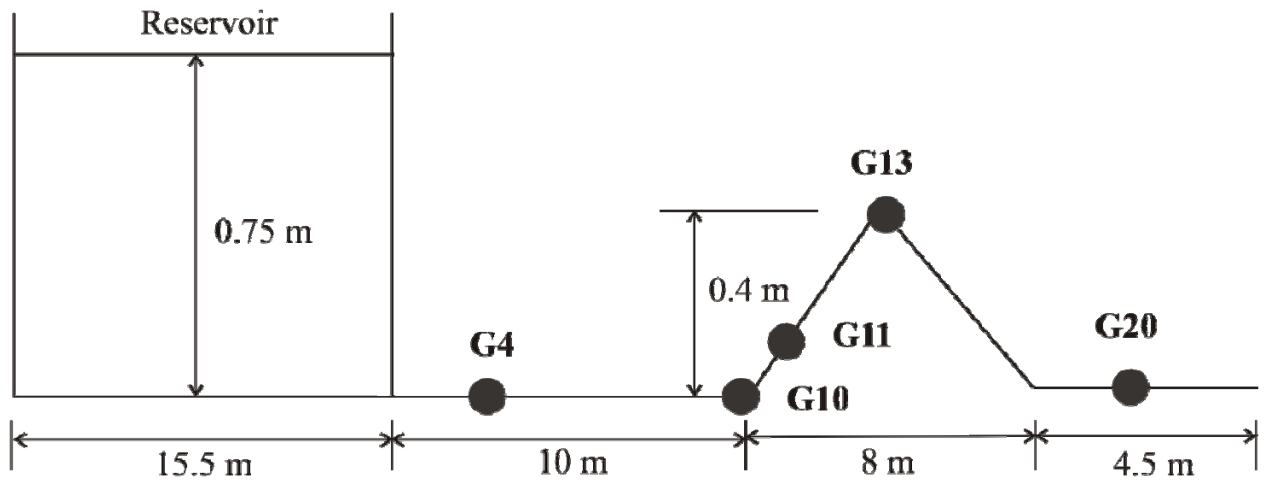


Fig. 6

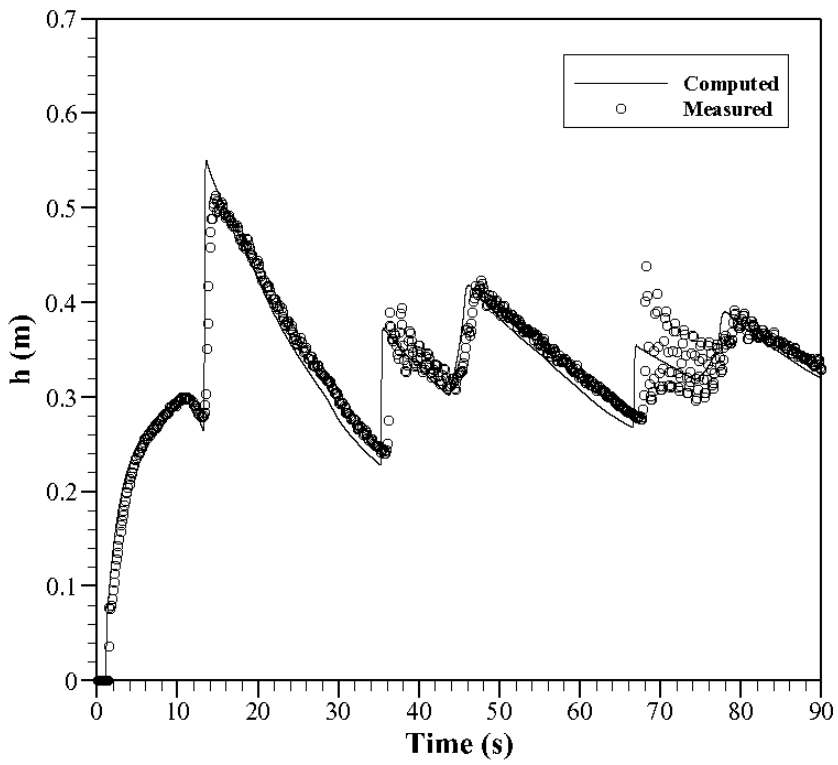


Fig. 7a

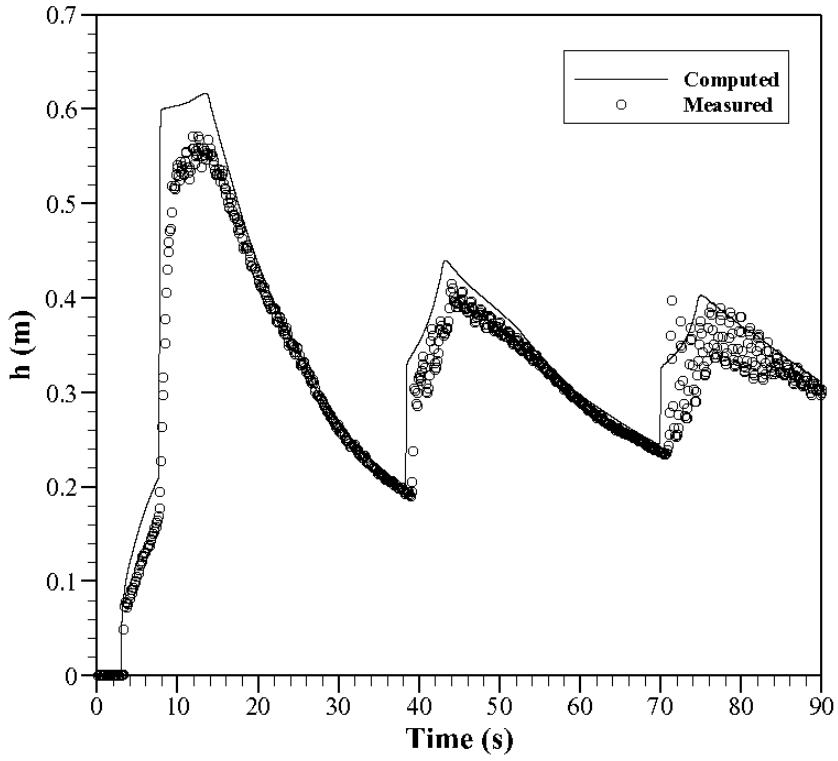


Fig. 7b

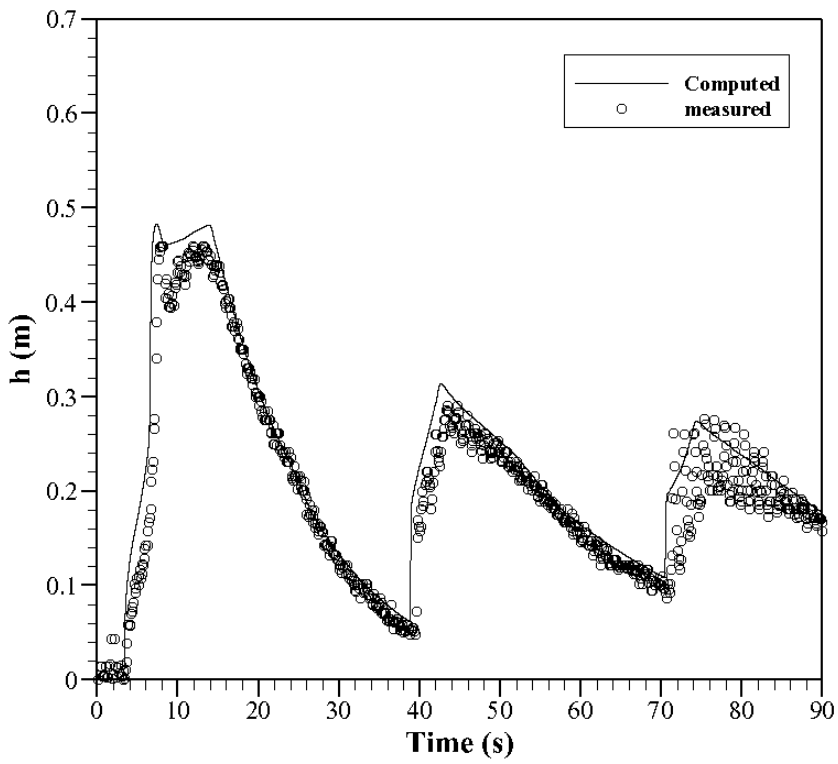


Fig. 7c

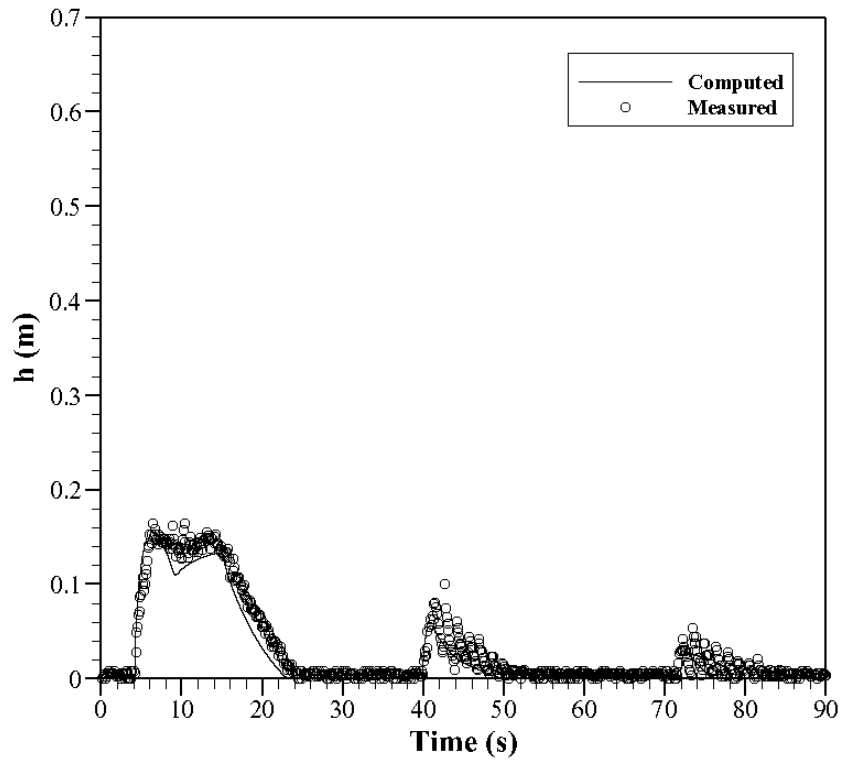


Fig. 7d

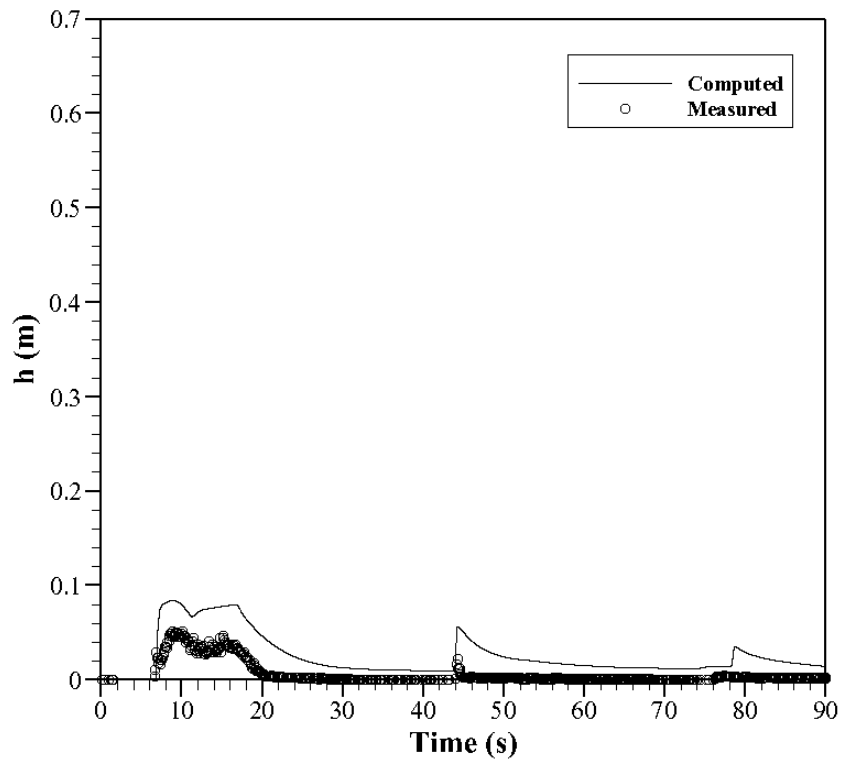


Fig. 7e

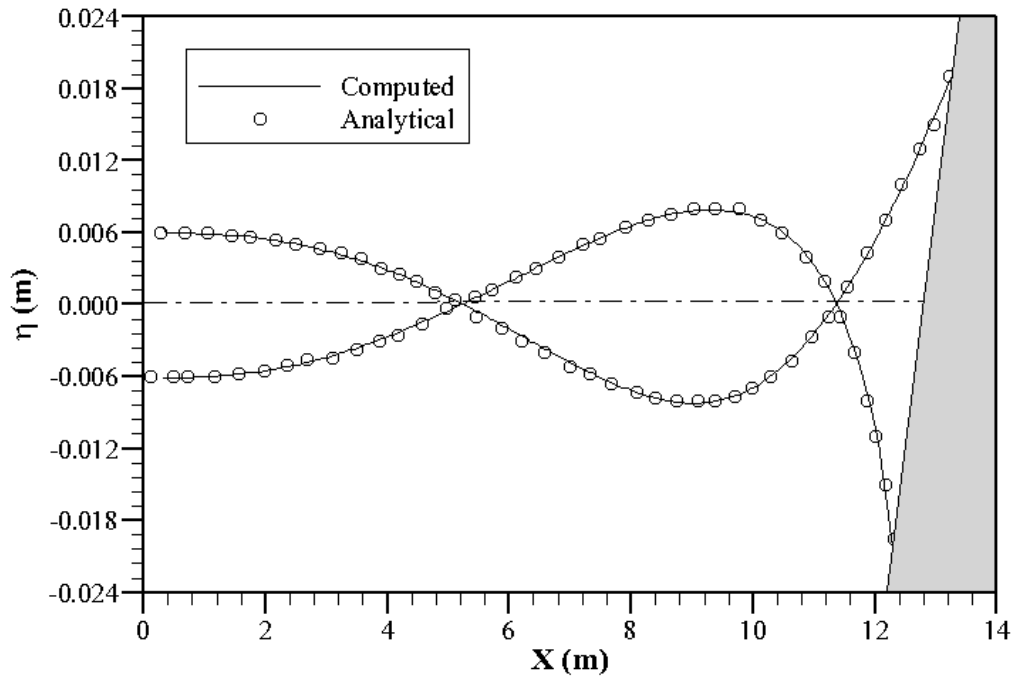


Fig. 8

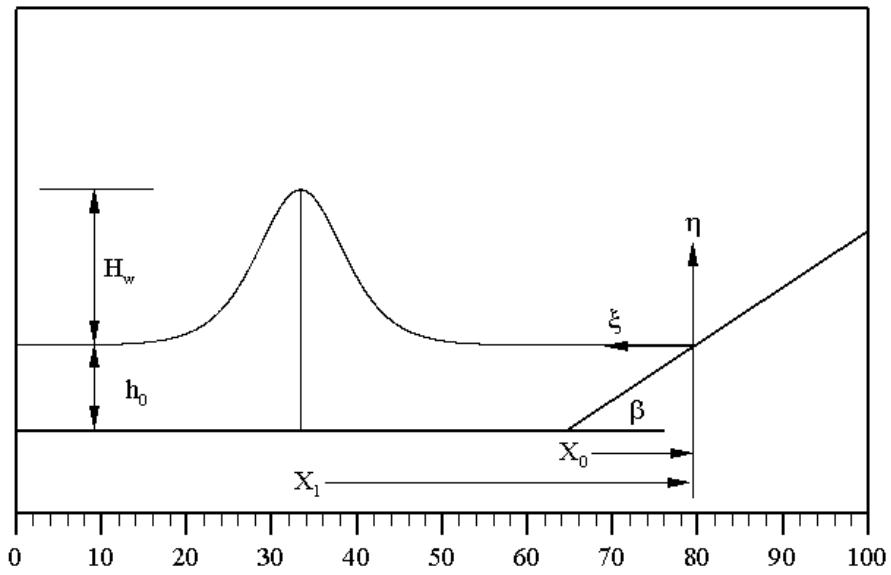


Fig. 9

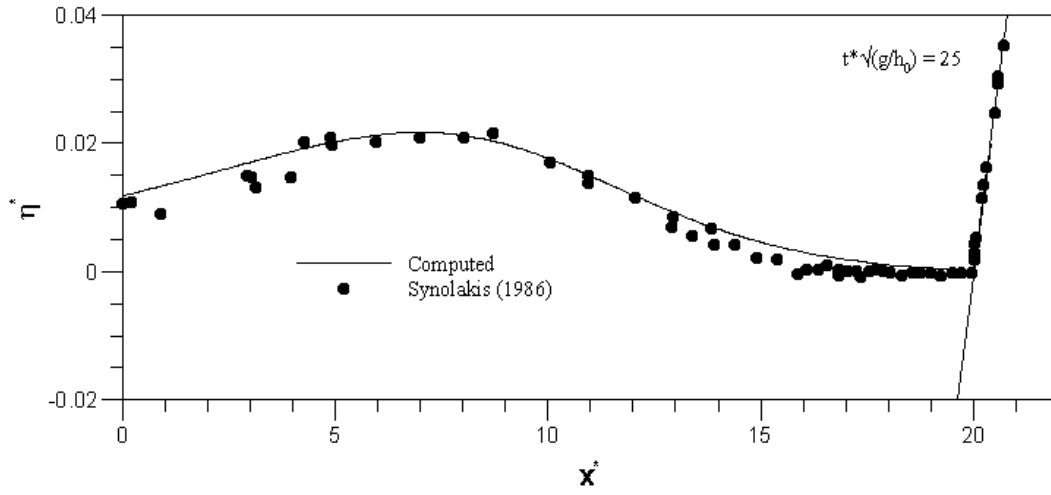


Fig. 10a

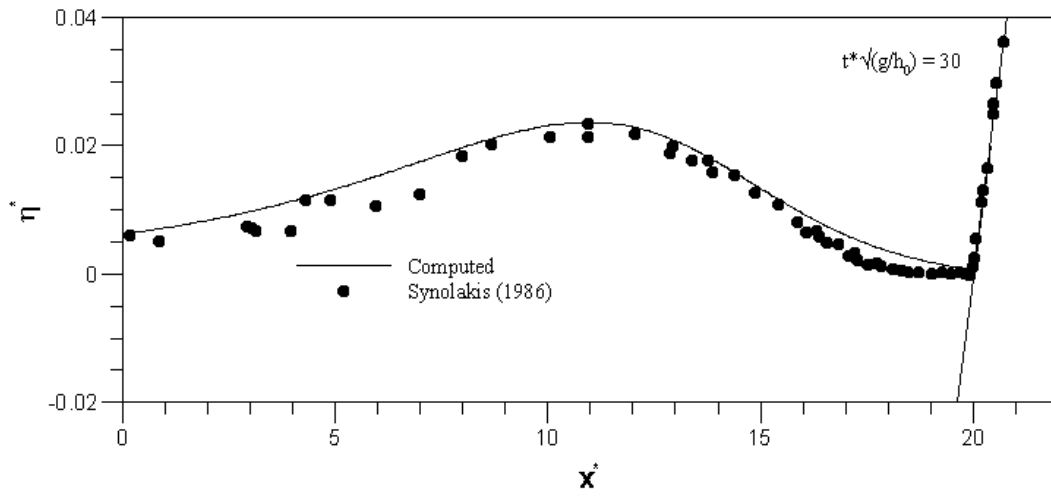


Fig. 10b

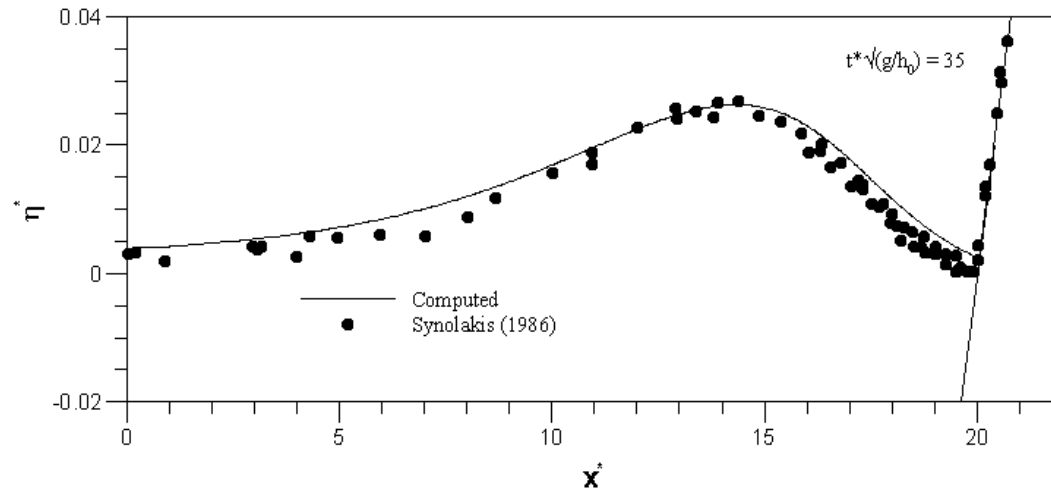


Fig. 10c

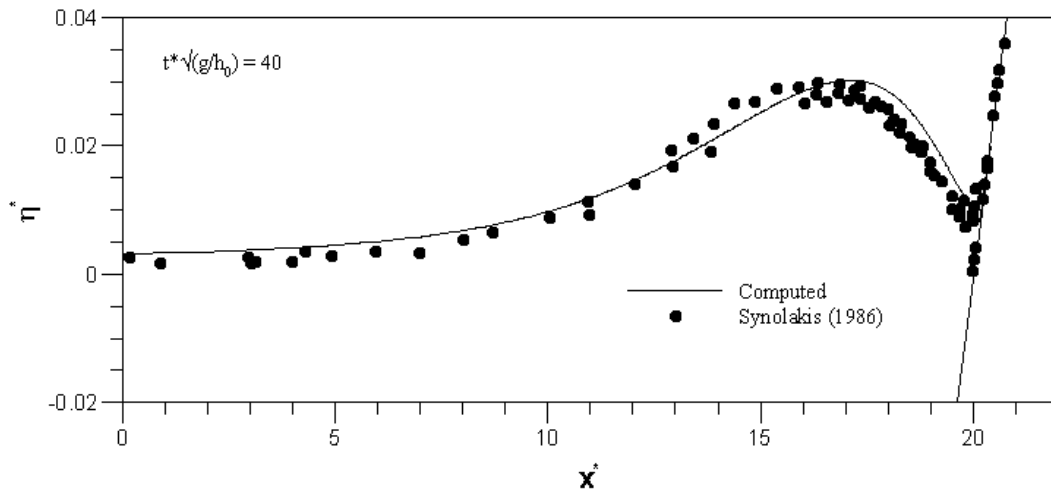


Fig. 10d

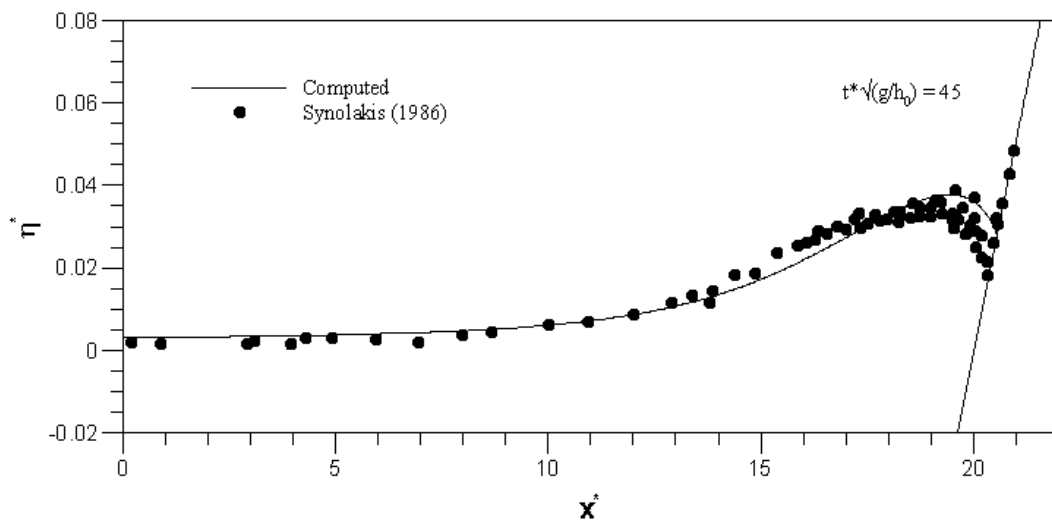


Fig. 10e

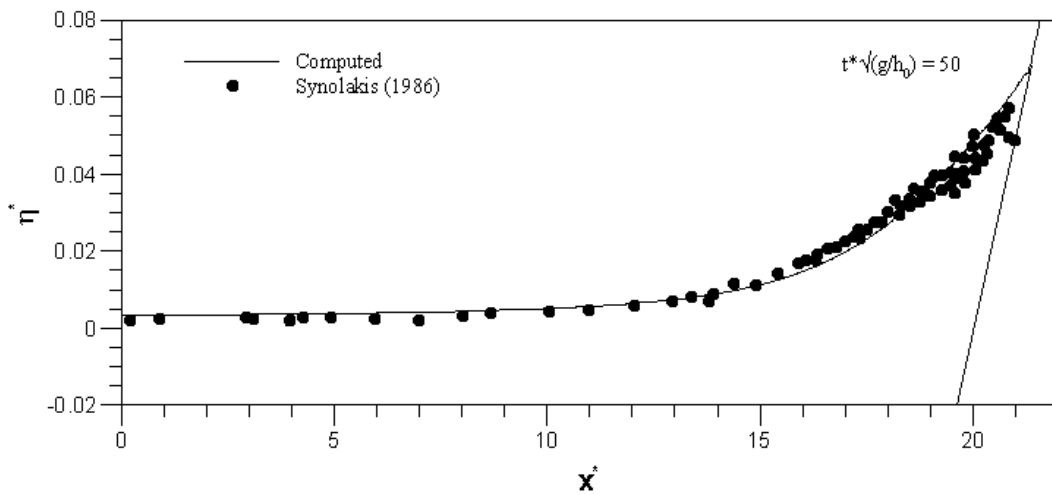


Fig. 10f

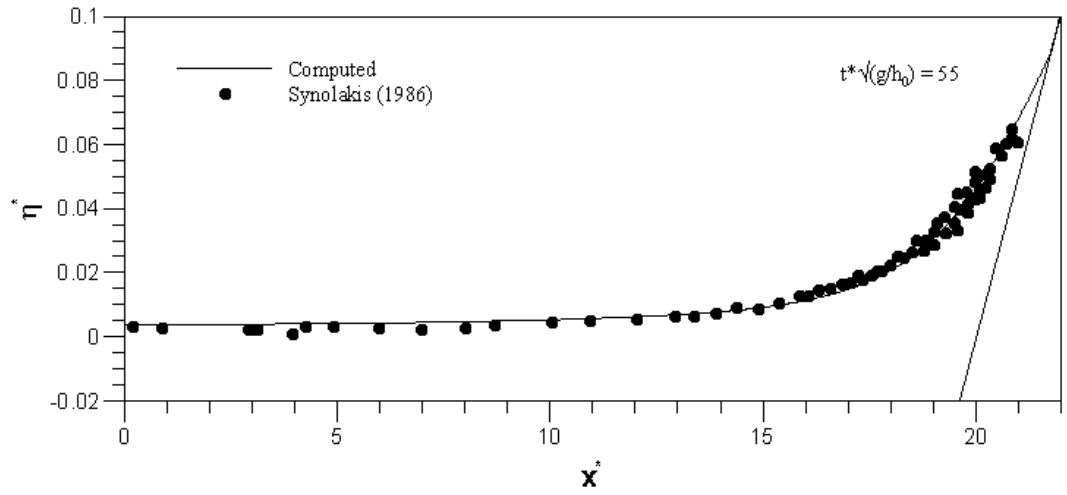


Fig. 10g

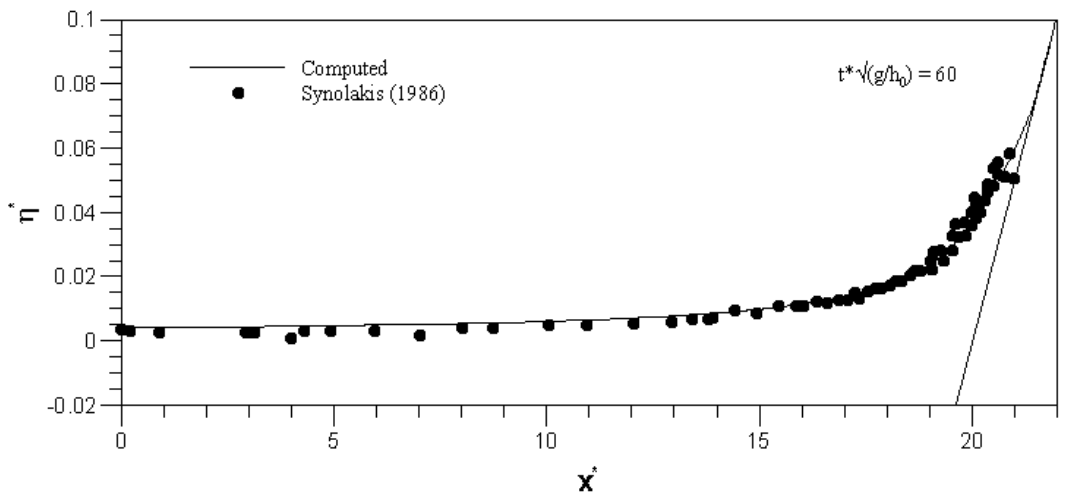


Fig. 10h

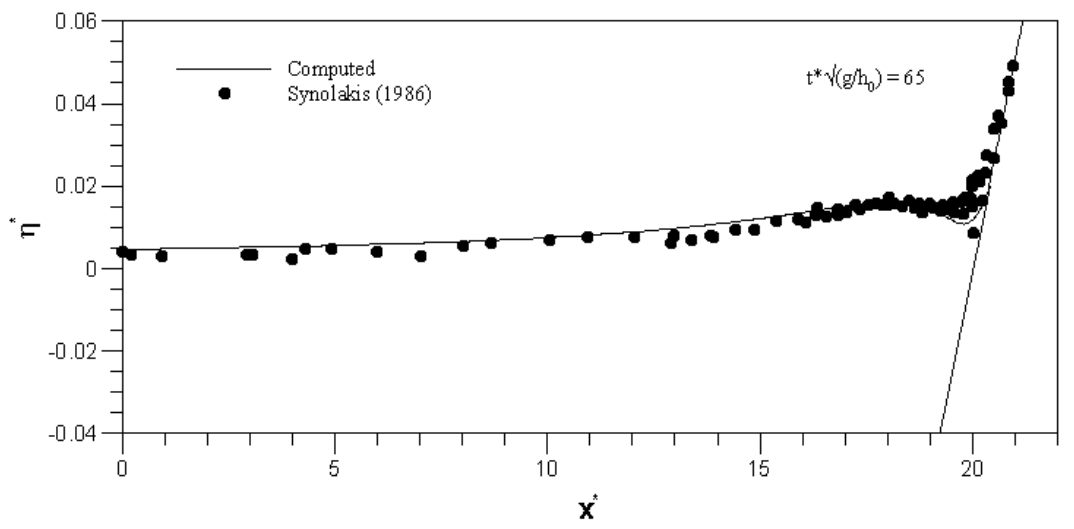


Fig. 10i

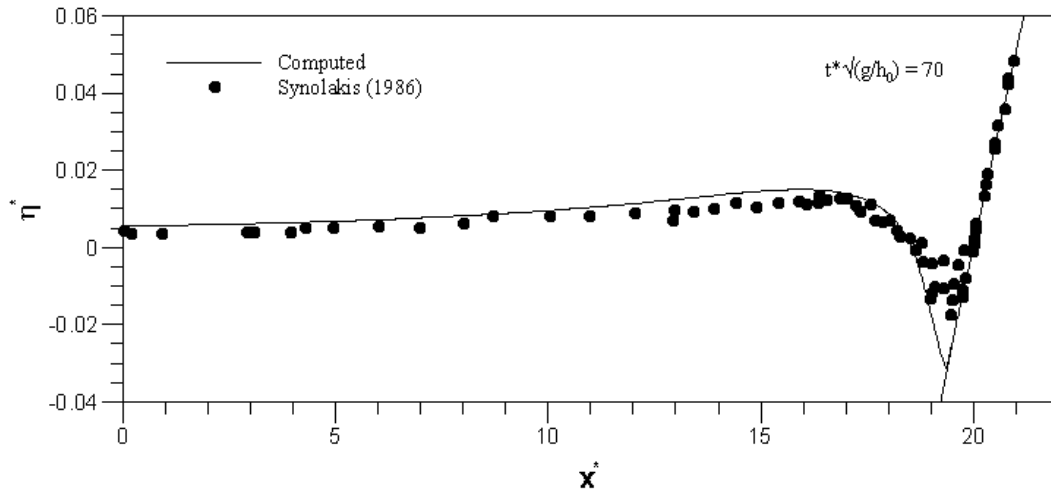


Fig. 10j

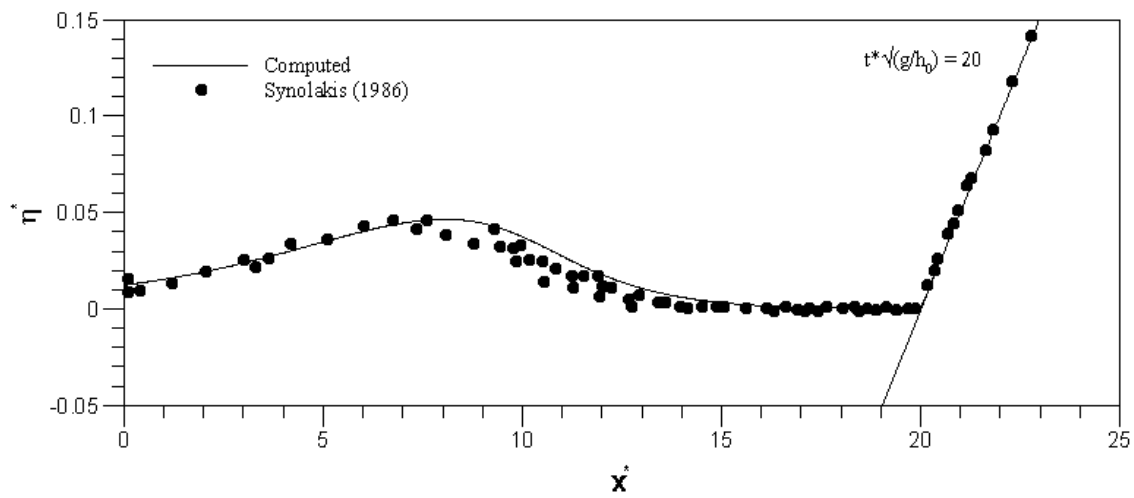


Fig. 11a

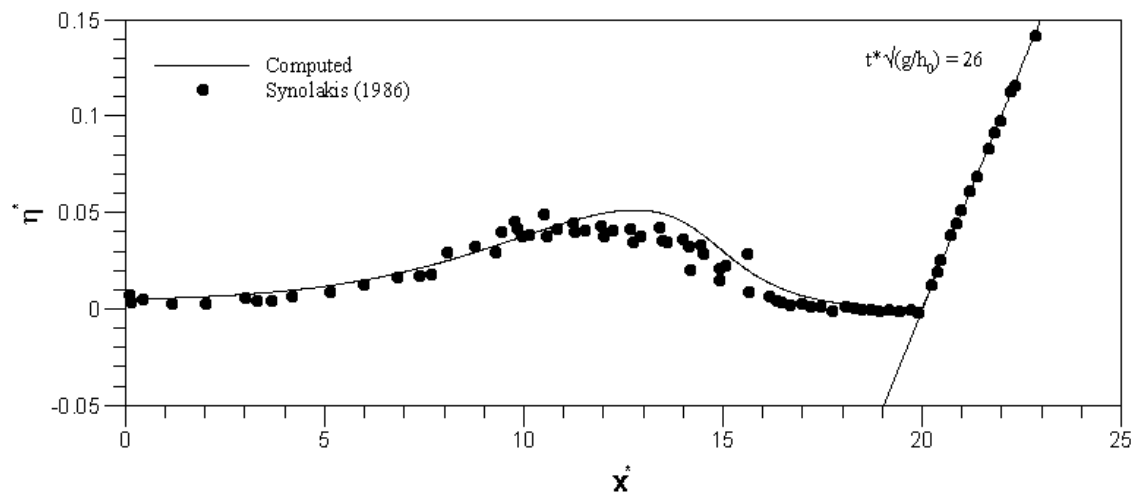


Fig. 11b

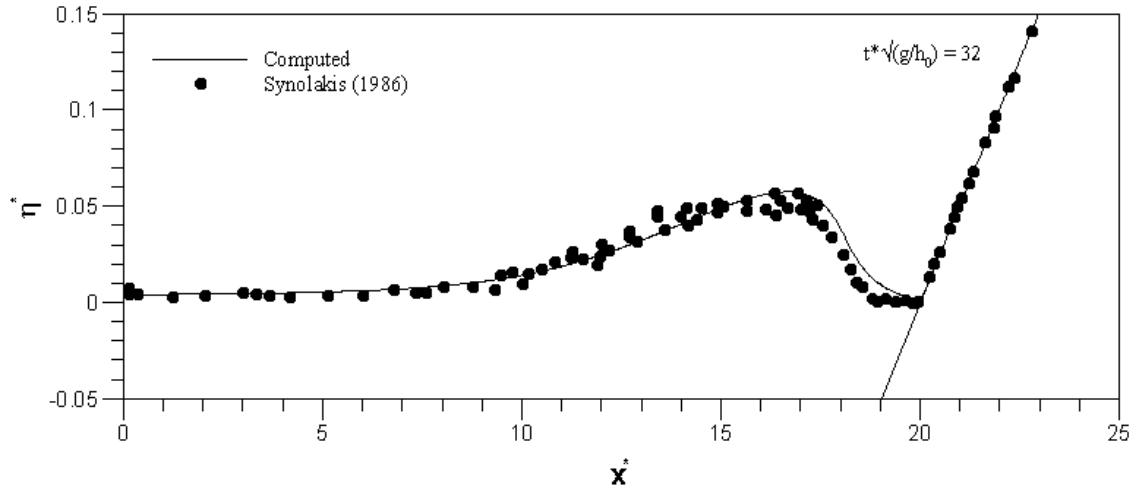


Fig. 11c

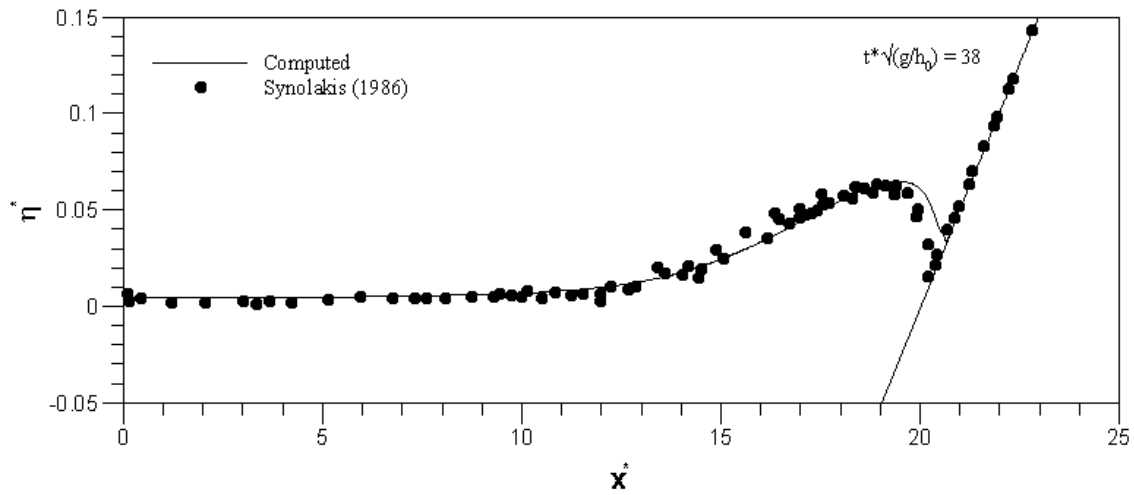


Fig. 11d

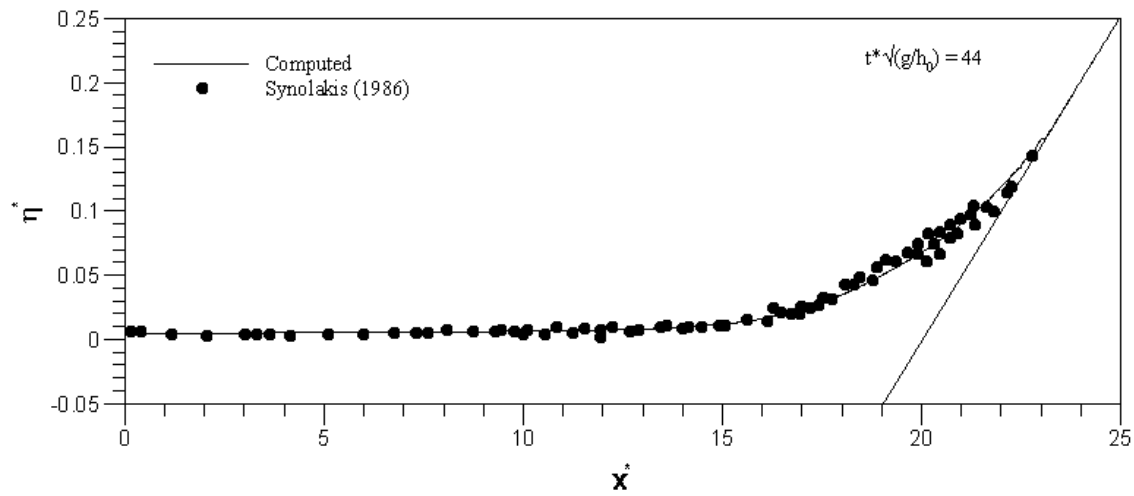


Fig. 11e

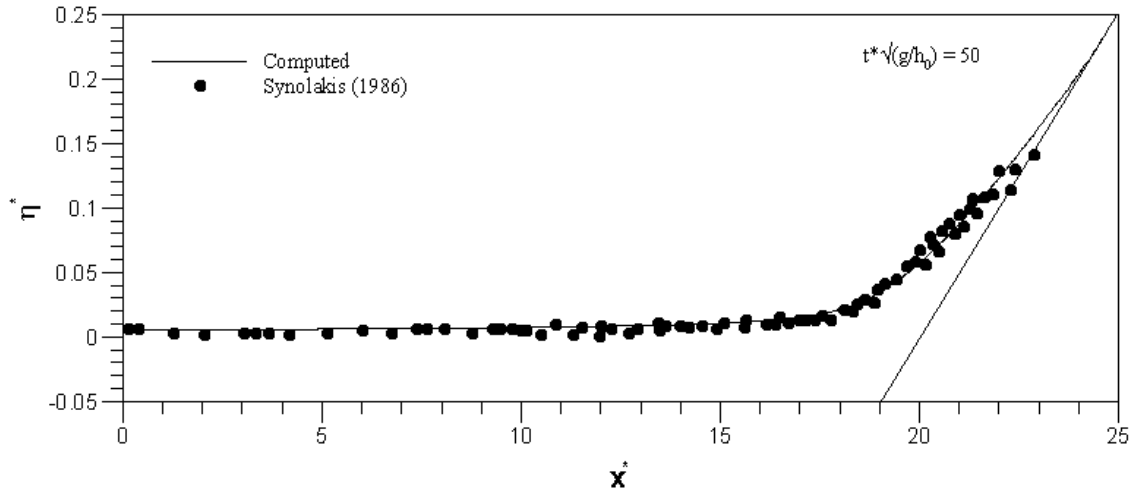


Fig. 11f

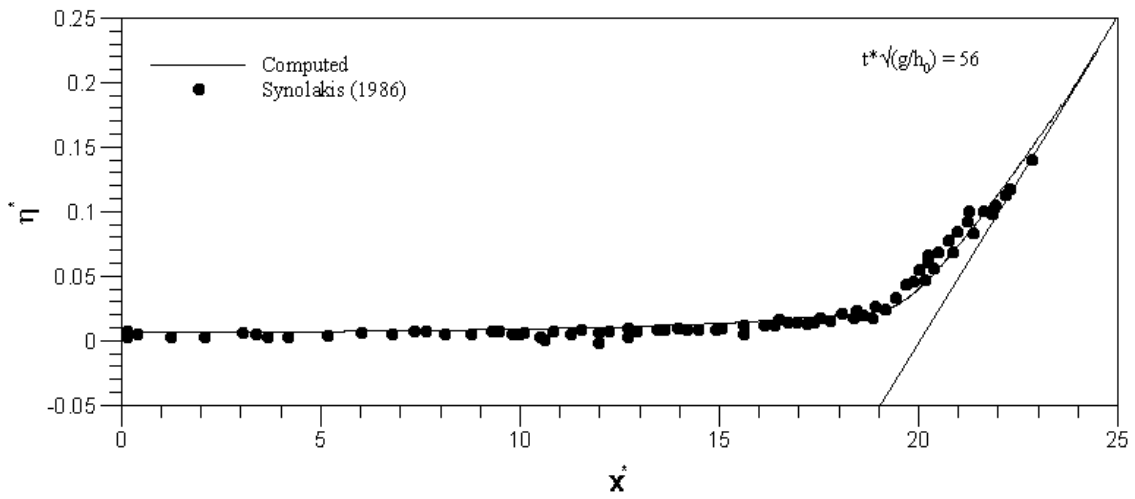


Fig. 11g

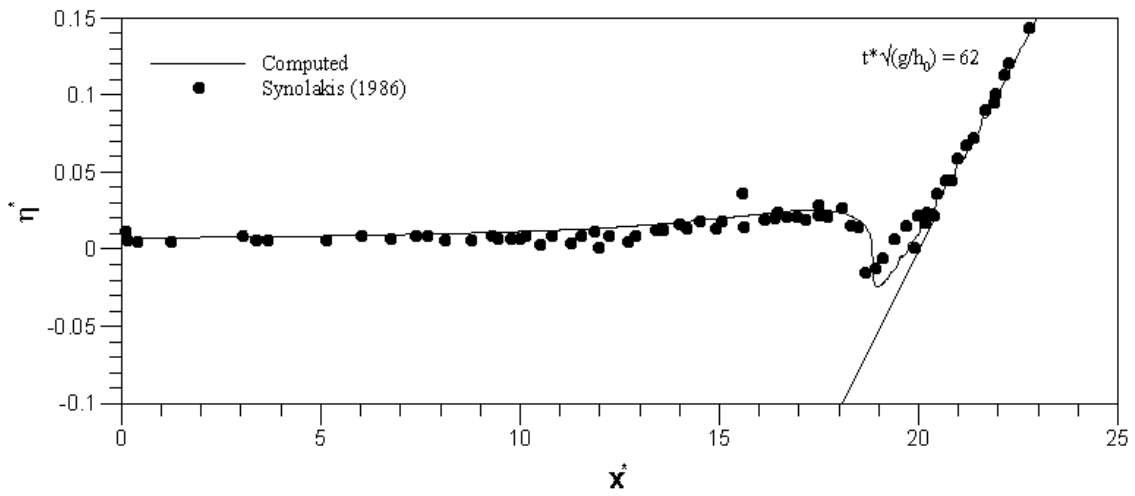


Fig. 11h

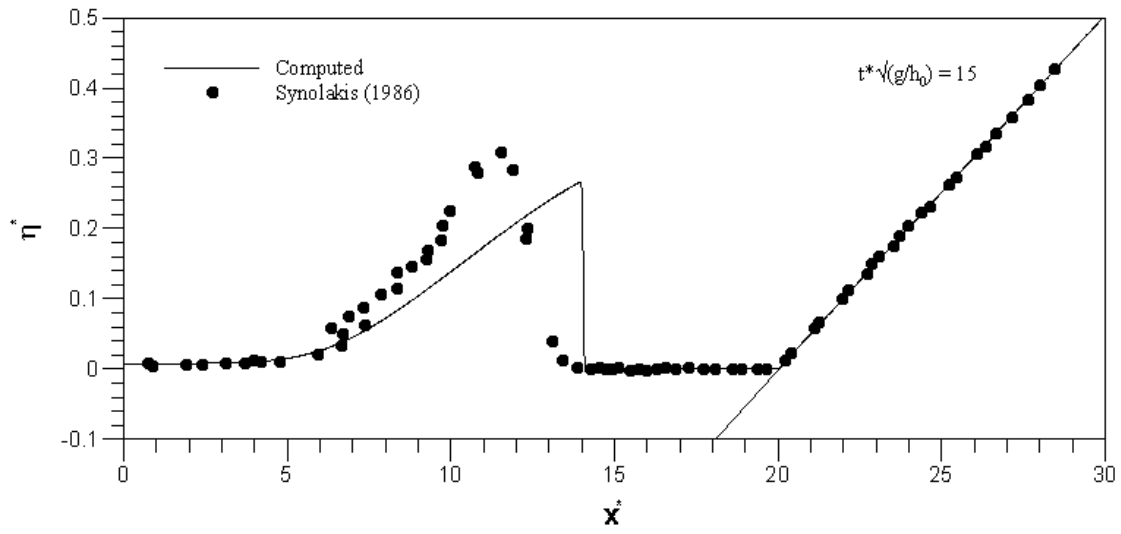


Fig. 12a

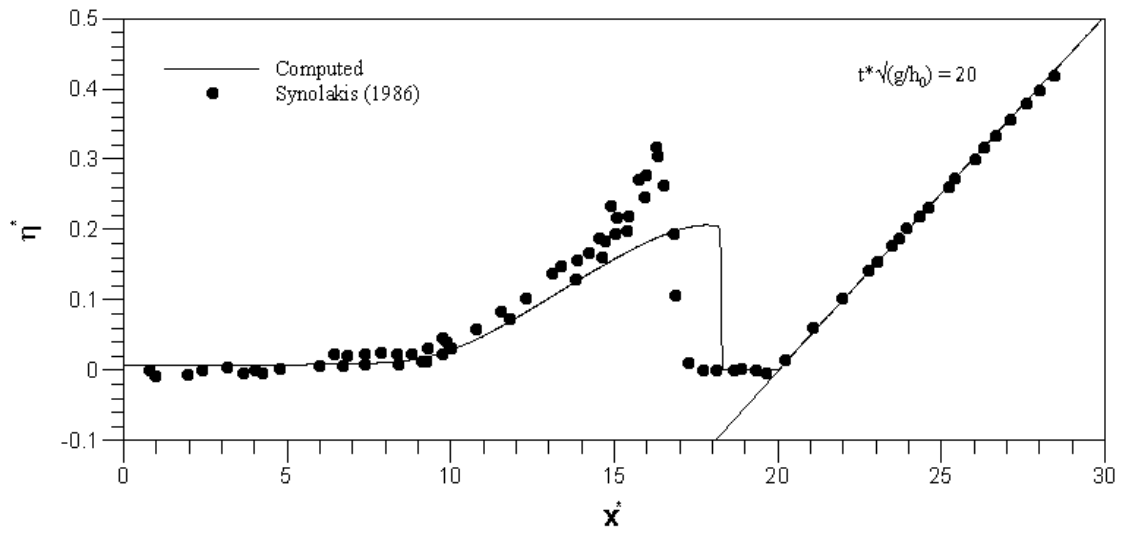


Fig. 12b

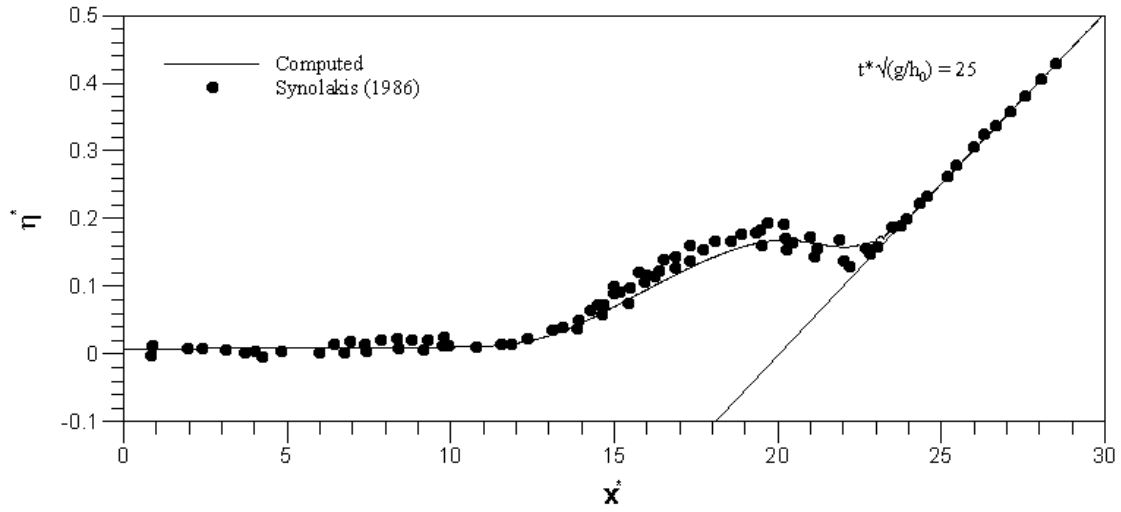


Fig. 12c

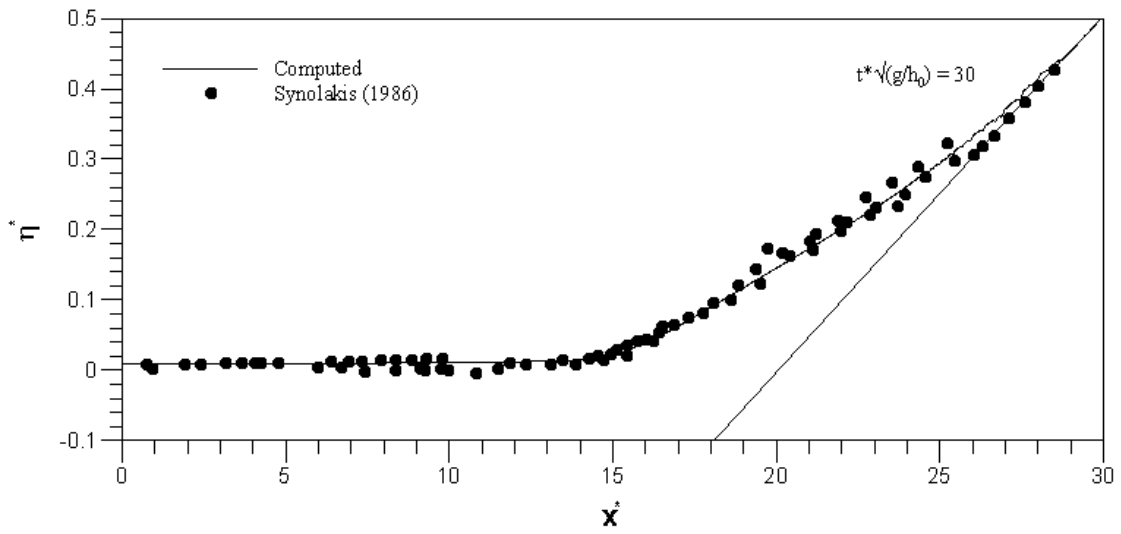


Fig. 12d

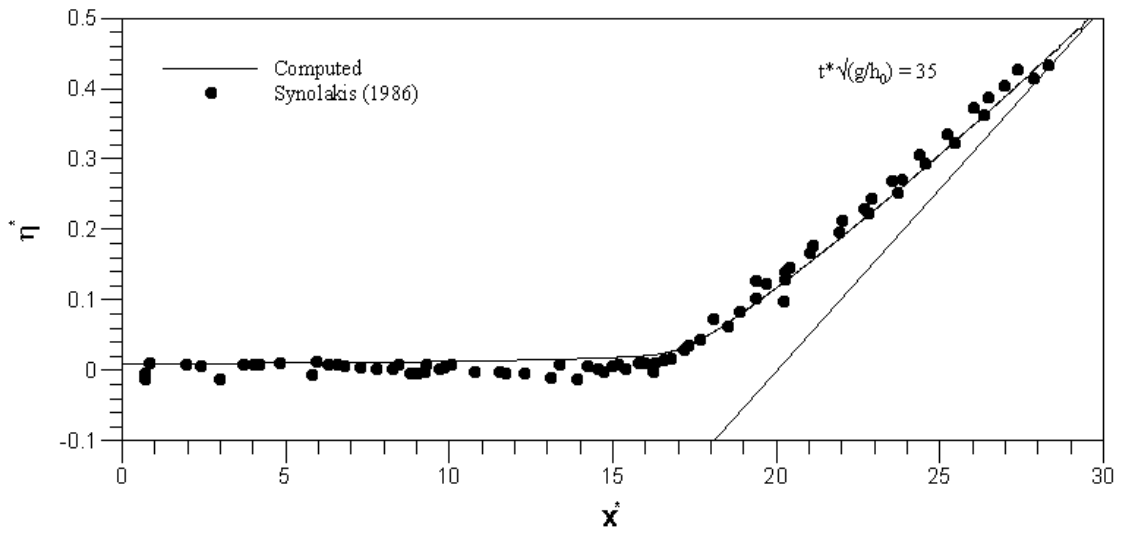


Fig. 12e

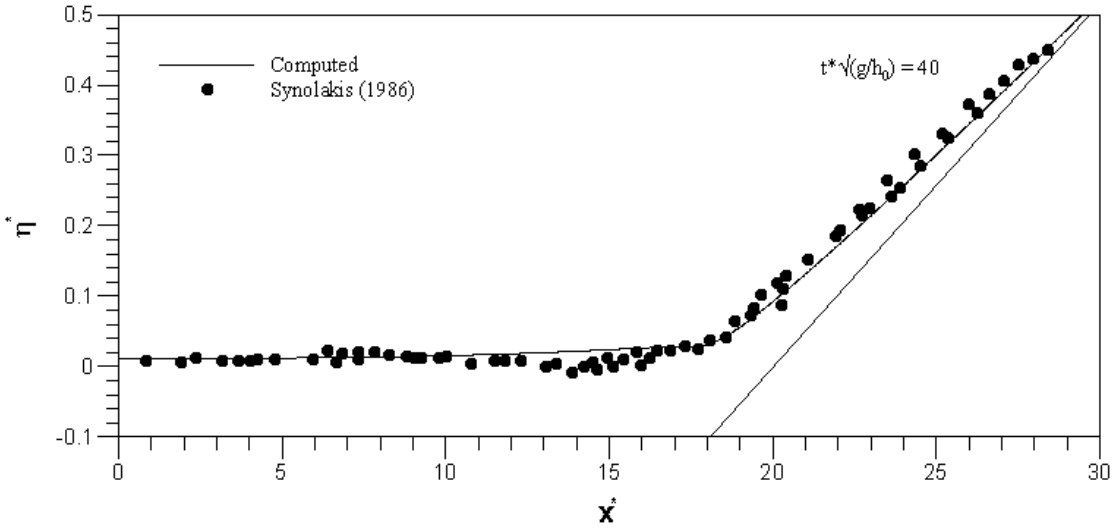


Fig. 12f

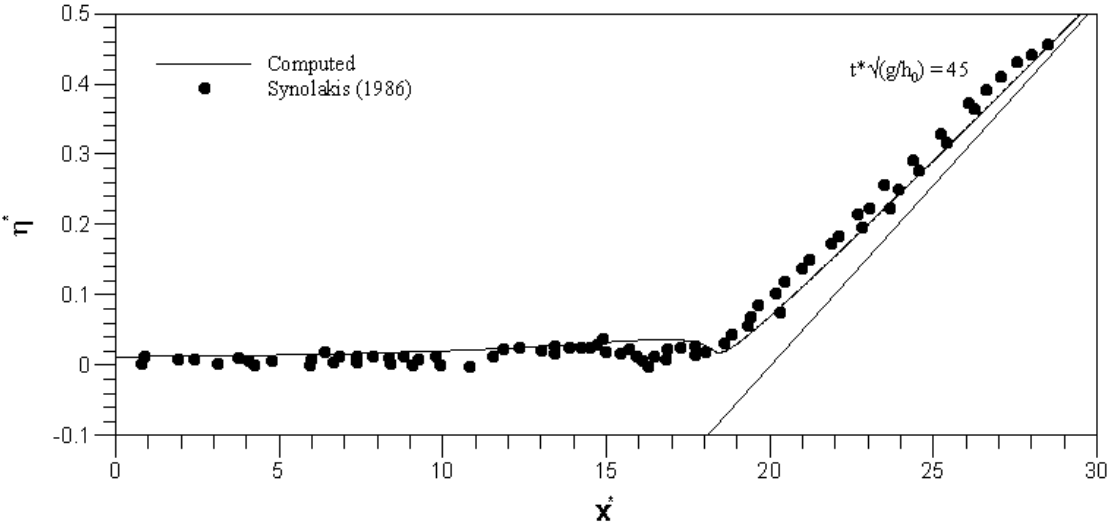


Fig. 12g

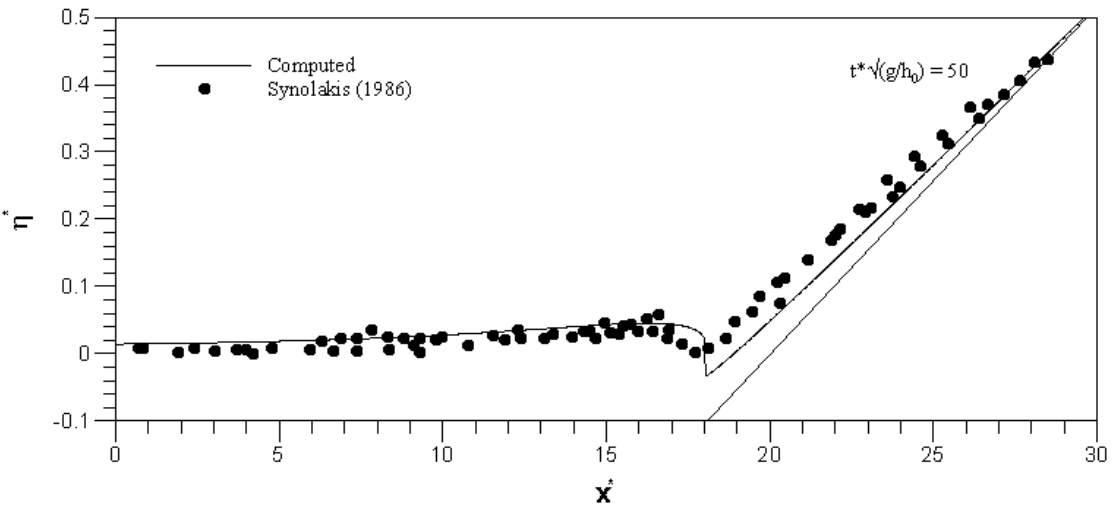


Fig. 12h

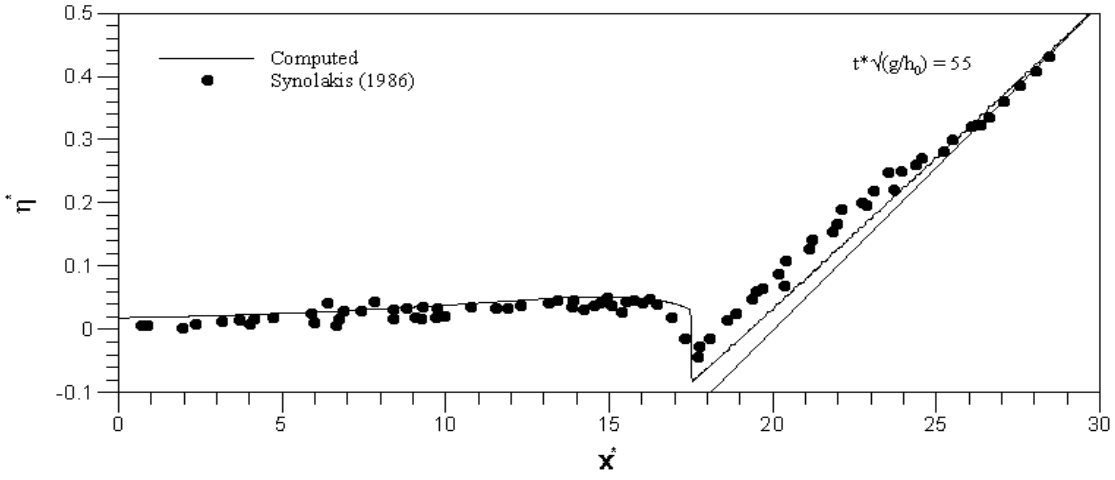


Fig. 12i

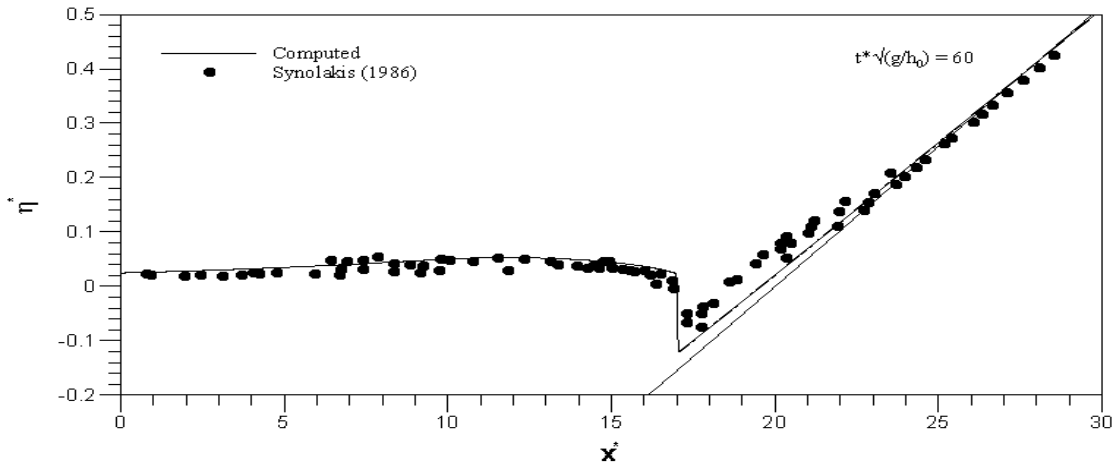


Fig. 12j

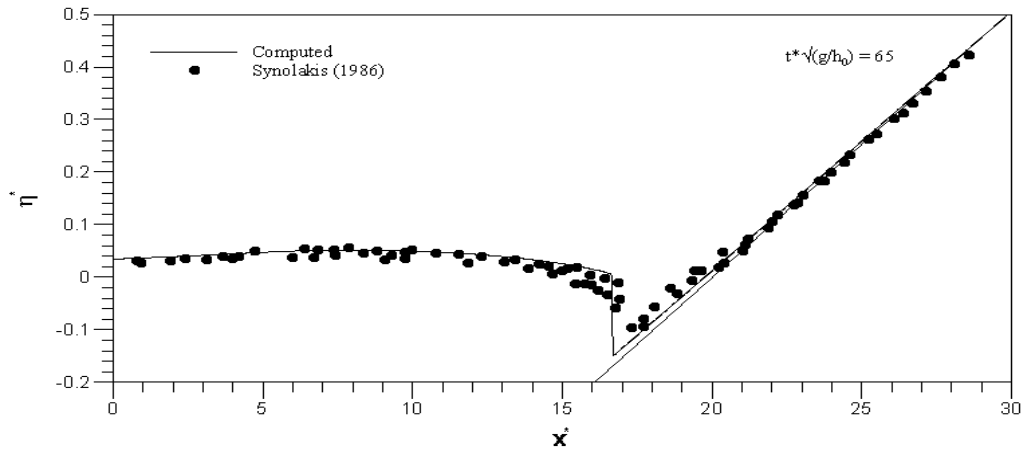


Fig. 12k

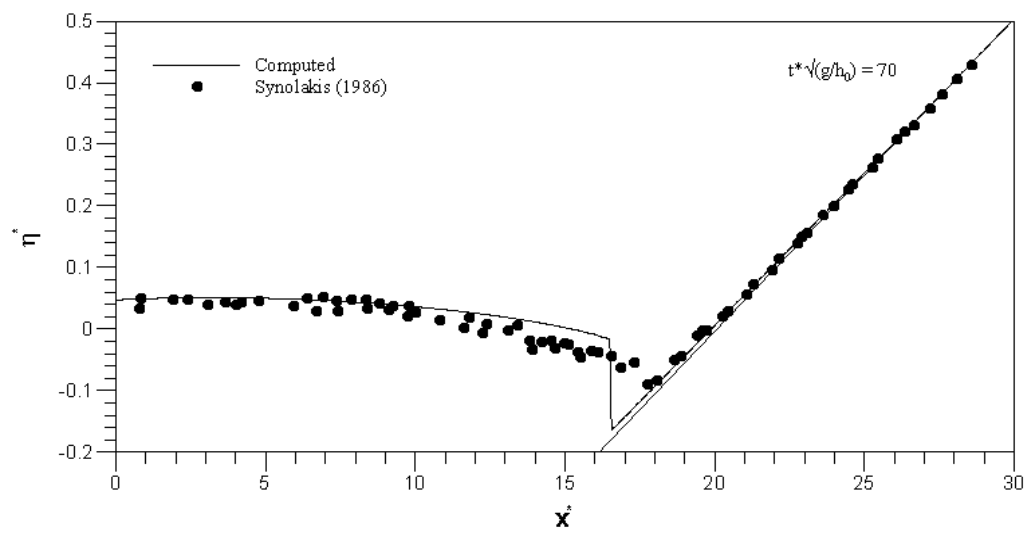


Fig. 12l

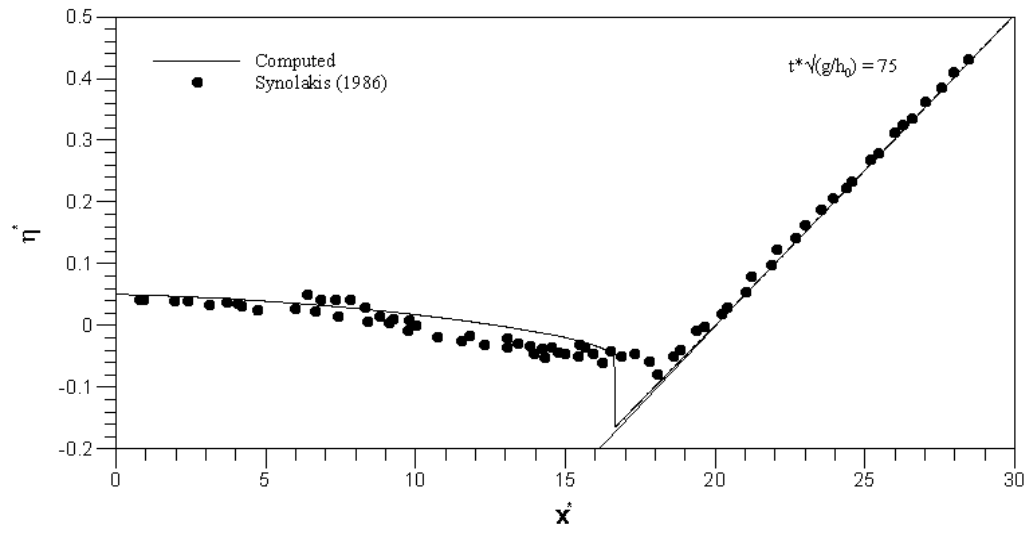


Fig. 12m

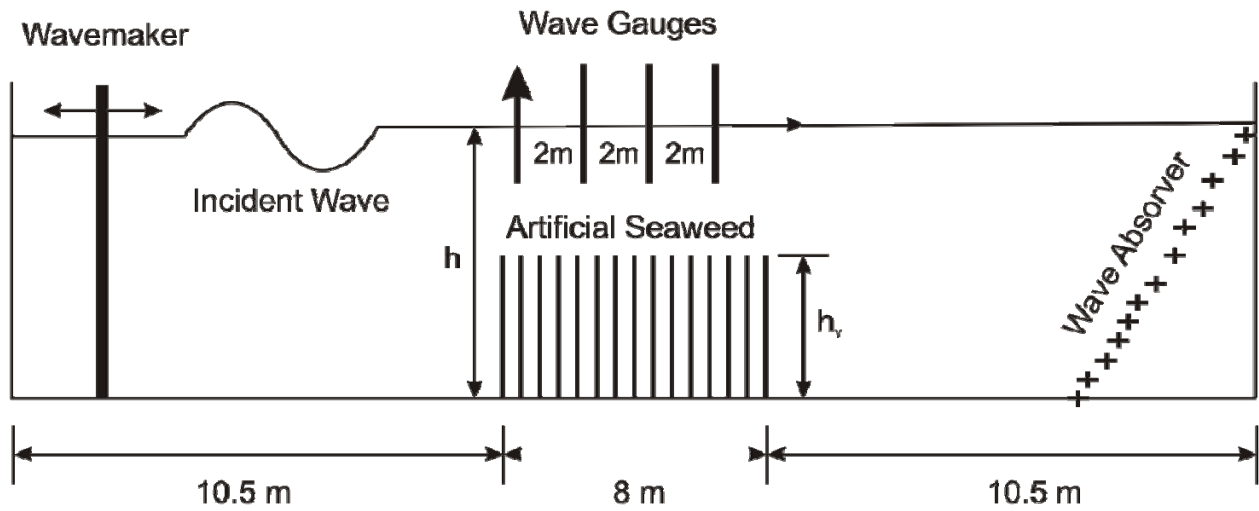


Fig. 13

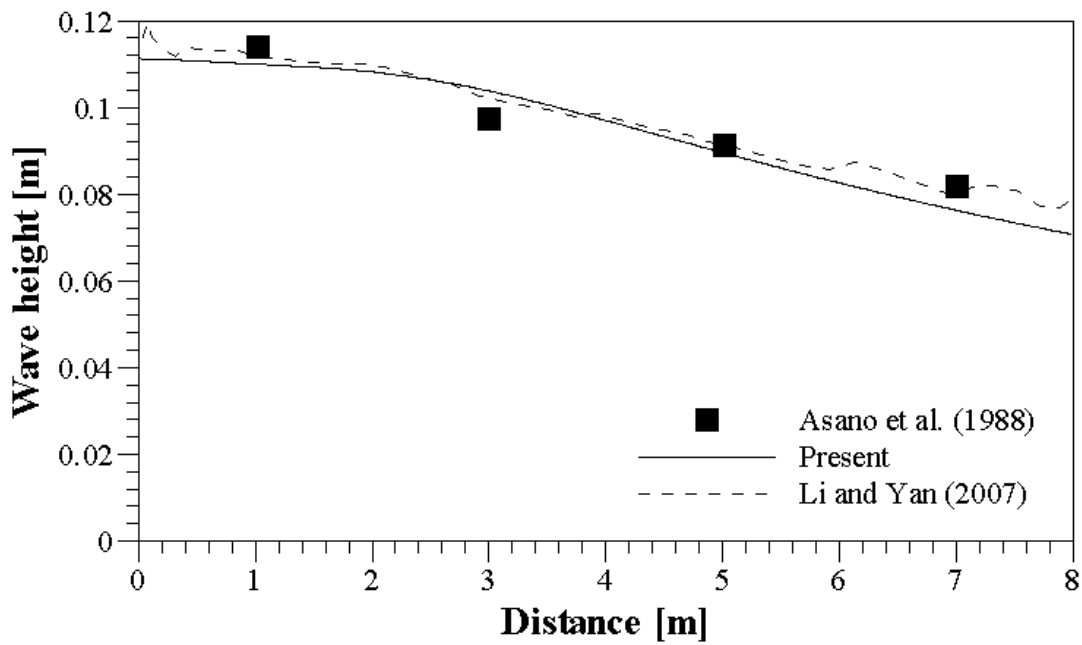


Fig. 14a

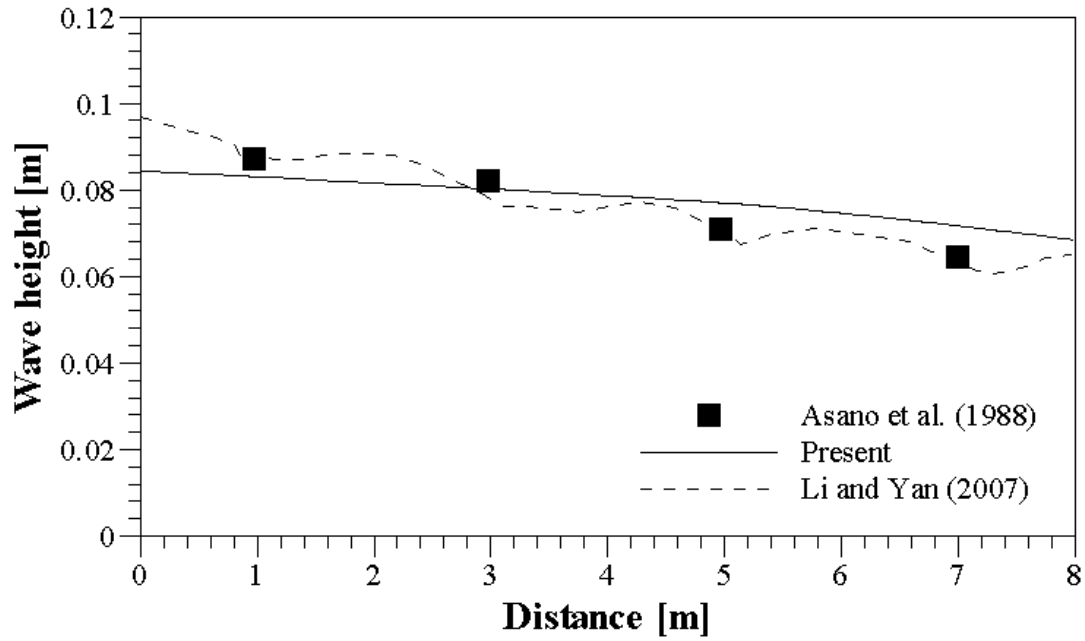


Fig. 14b

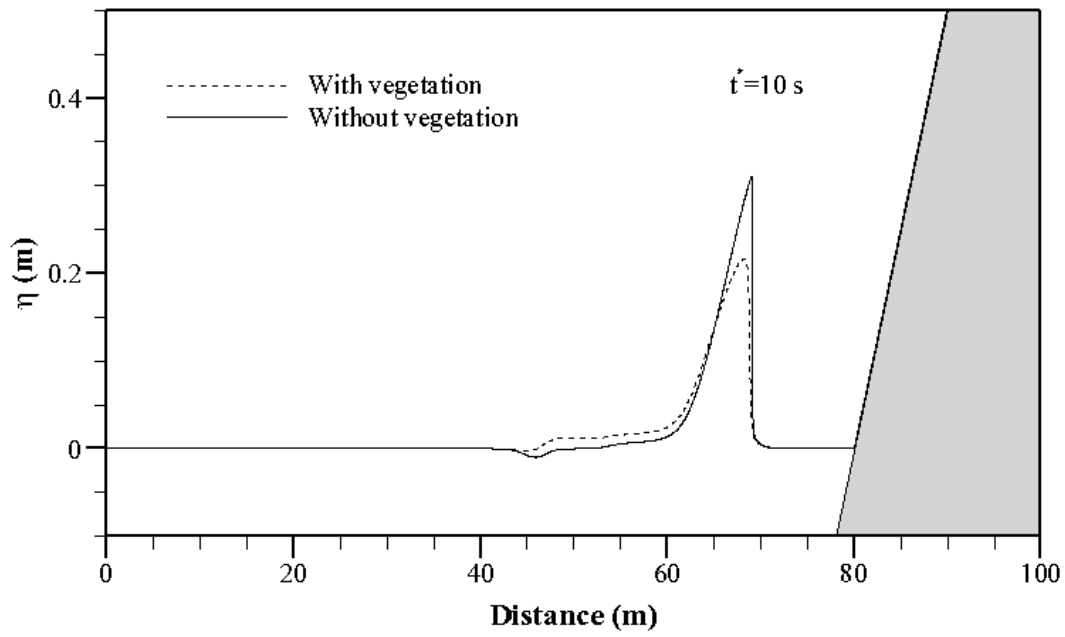


Fig. 15a

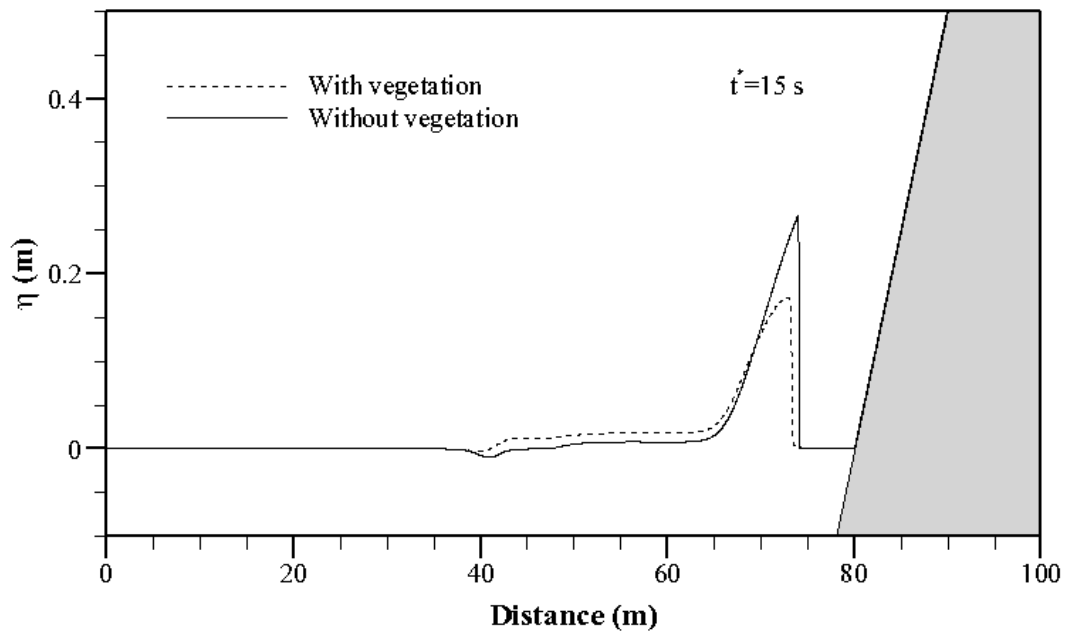


Fig. 15b

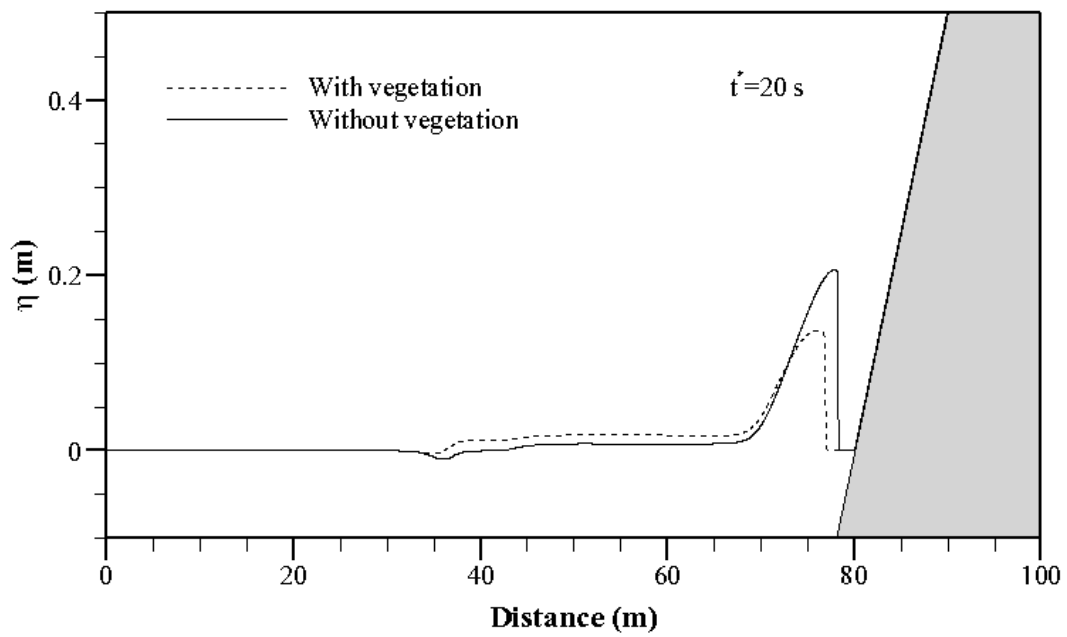


Fig. 15c

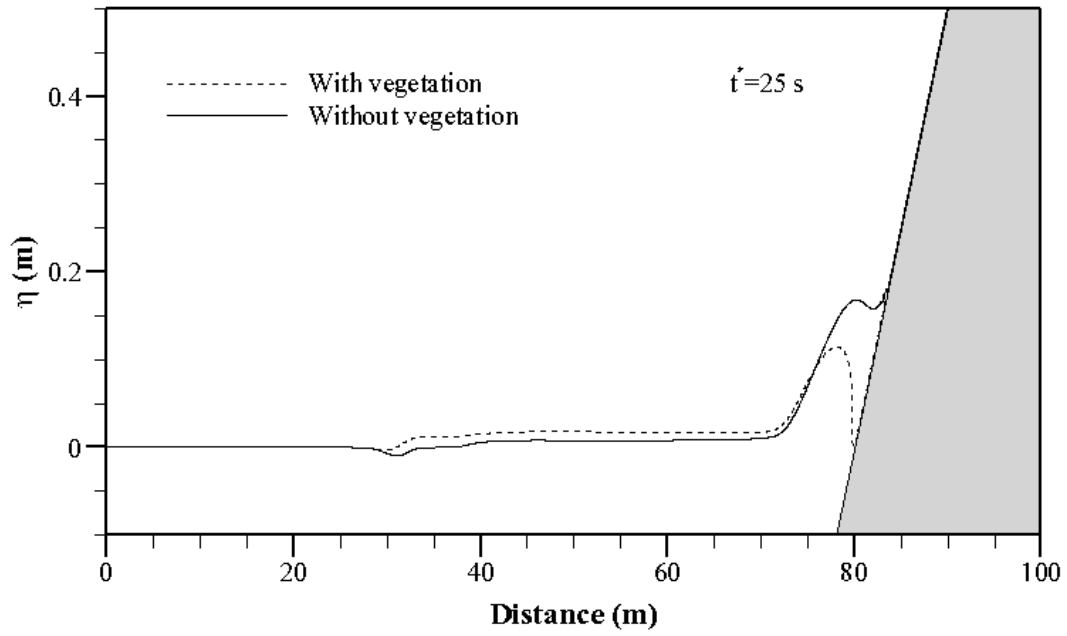


Fig. 15d

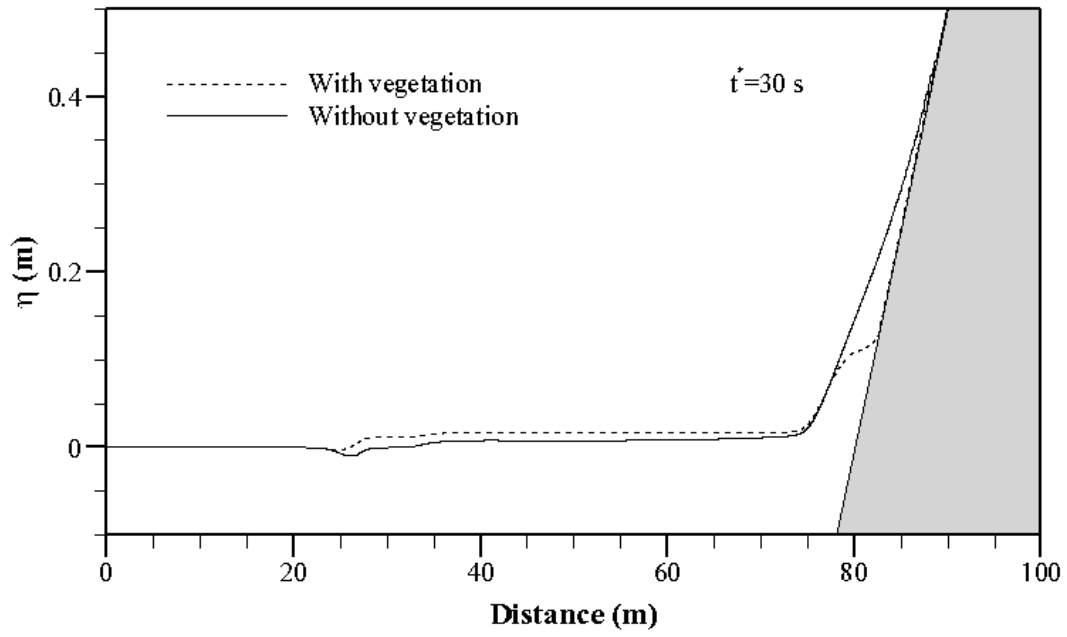


Fig. 15e

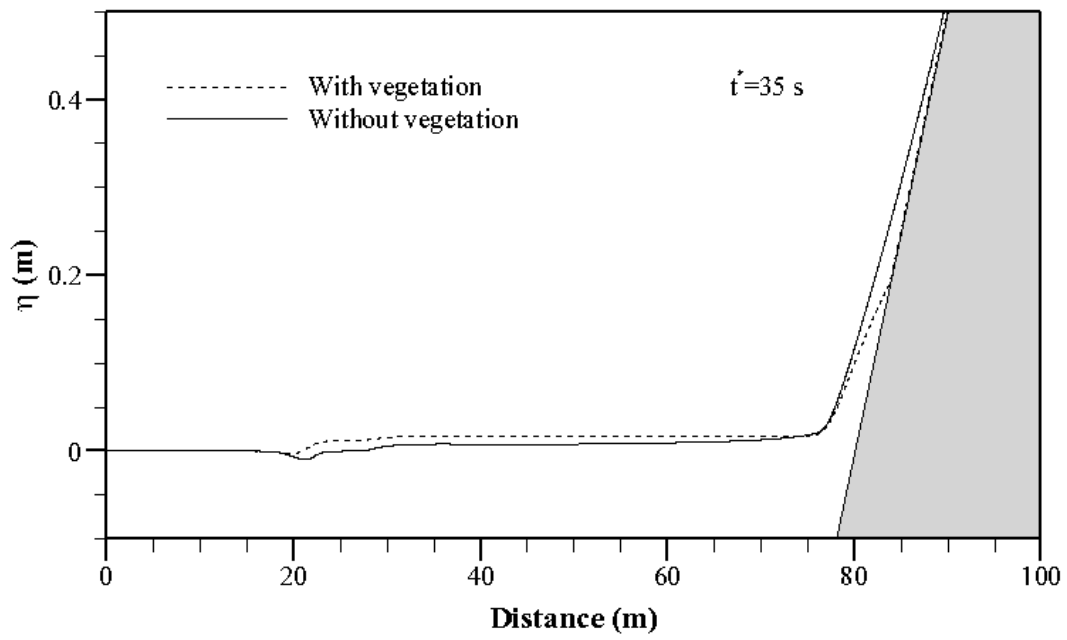


Fig. 15f

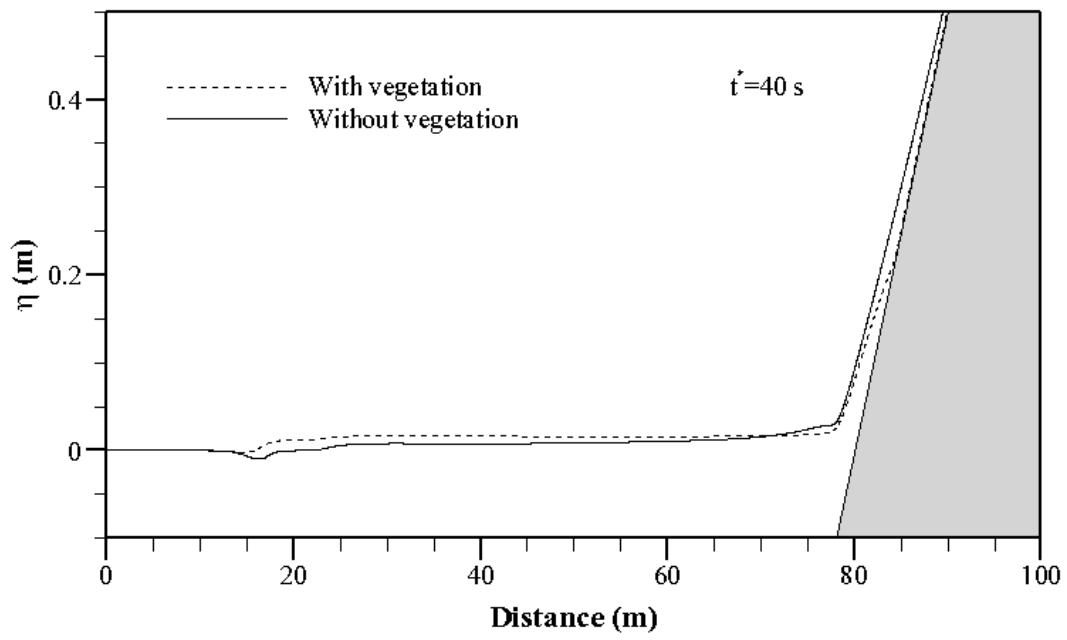


Fig. 15g

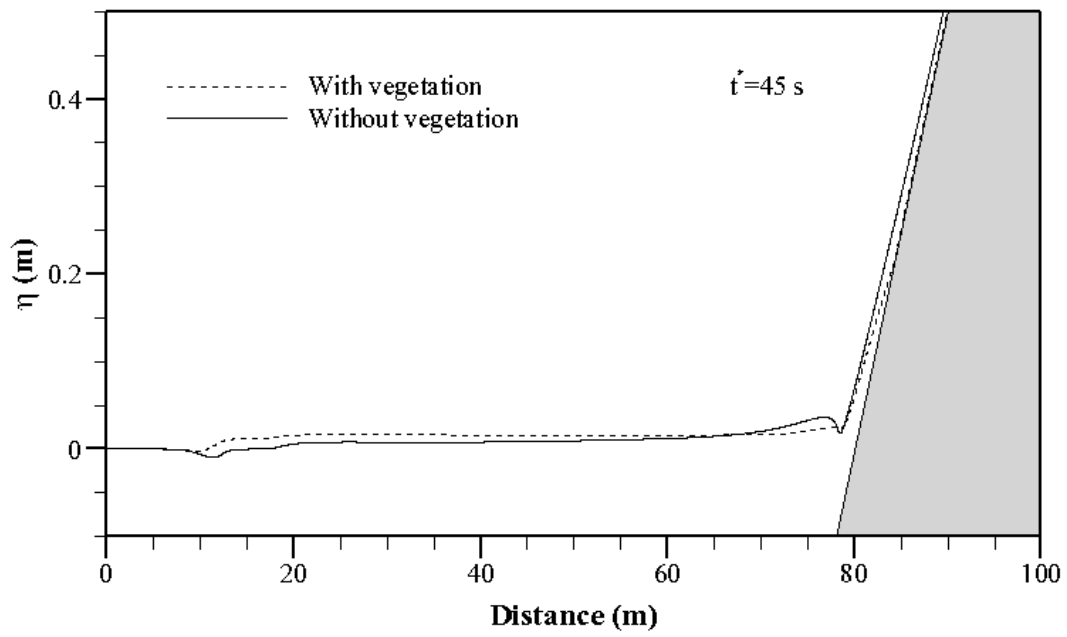


Fig. 15h

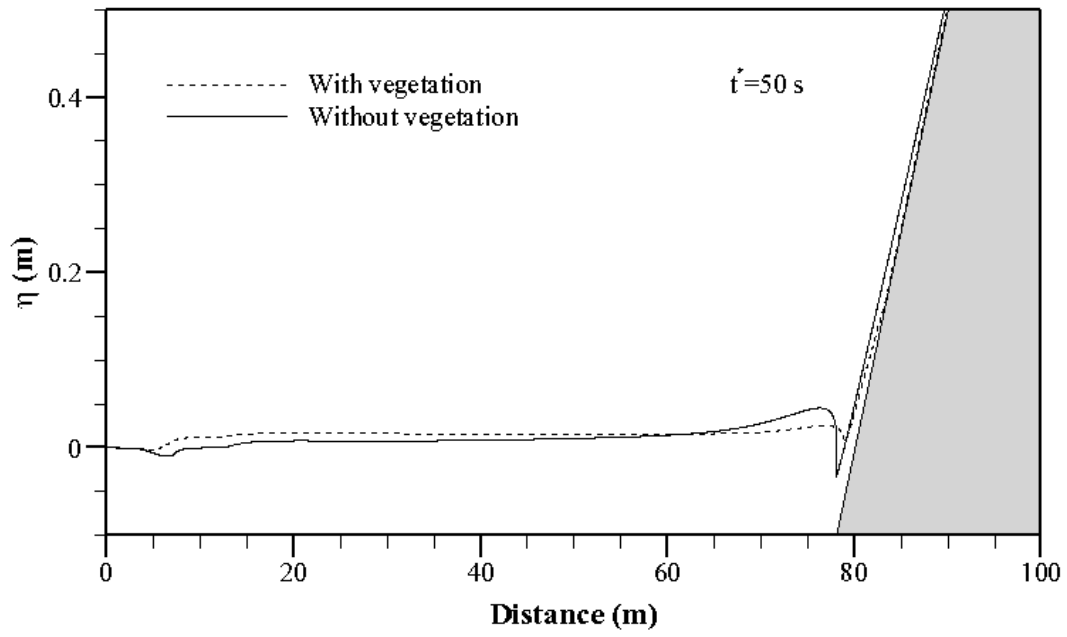


Fig. 15i

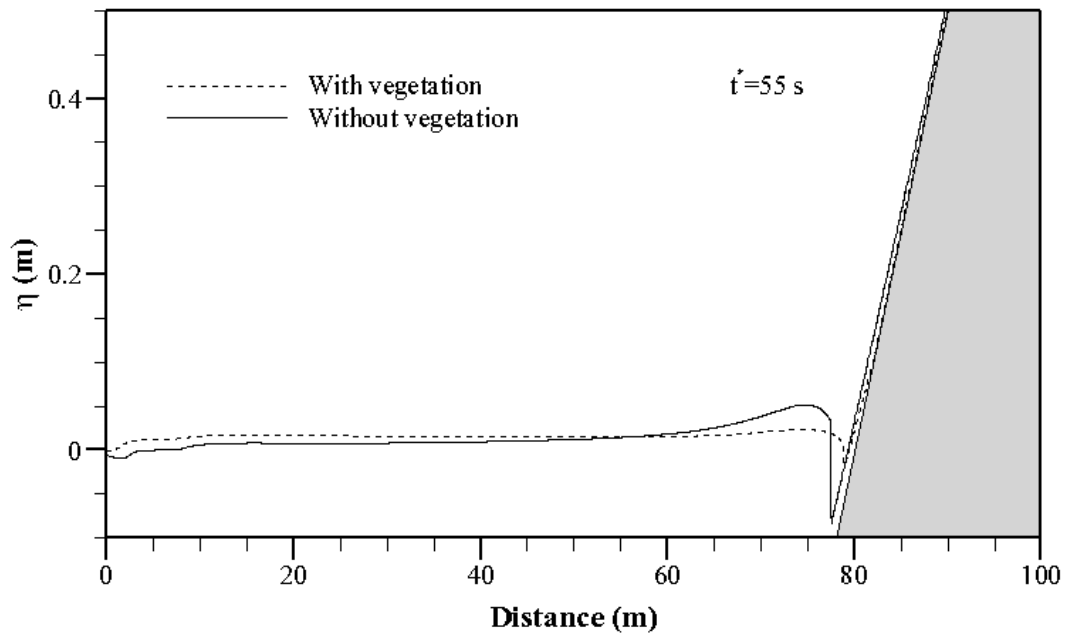


Fig. 15j